## Jitter Radiation as an Alternative Mechanism for the Nonthermal X-Ray Emission of Cassiopeia A

Greco, E.; Vink, J.; Ellien, A.; Ferrigno, C.

# Jitter Radiation as an Alternative Mechanism for the Nonthermal X-Ray Emission of Cassiopeia A

Emanuele Greco[1] , Jacco Vink[1] , Amael Ellien[1] , and Carlo Ferrigno[2,3]

[1] Anton Pannekoek Institute for Astronomy & GRAPPA, University of Amsterdam, Science Park 904, 1098 XH Amsterdam, The Netherlands; e.greco@uva.nl
[2] Department of Astronomy, University of Geneva, Chemin d'Ecogia 16, CH-1290 Versoix, Switzerland
[3] INAF, Osservatorio Astronomico di Brera, Via E. Bianchi 46, I-23807 Merate, Italy

## Abstract

Synchrotron radiation from relativistic electrons is usually invoked as responsible for the nonthermal emission observed in supernova remnants. Diffusive shock acceleration is the most popular mechanism to explain the process of particles acceleration and within its framework a crucial role is played by the turbulent magnetic field. However, the standard models commonly used to fit X-ray synchrotron emission do not take into account the effects of turbulence in the shape of the resulting photon spectra. An alternative mechanism that properly includes such effects is the jitter radiation, which provides for an additional power law beyond the classical synchrotron cutoff. We fitted a jitter spectral model to Chandra, NuSTAR, SWIFT/BAT, and INTEGRAL/ISGRI spectra of Cassiopeia A (Cas A) and found that it describes the X-ray soft-to-hard range better than any of the standard cutoff models. The jitter radiation allows us to measure the index of the magnetic turbulence spectrum $\nu_B$ and the minimum scale of the turbulence $\lambda_{\min}$ across several regions of Cas A, with best-fit values $\nu_B \sim 2 - 2.4$ and $\lambda_{\min} \lesssim 100$ km.

## 1. Introduction

It is generally accepted that particle acceleration at the shock fronts of supernova remnants (SNRs) is the result of diffusive shock acceleration (DSA; Bell 1978; Malkov & O'C Drury 2001). According to DSA, charged particles repeatedly cross the shock front back and forth due to the magnetic-field irregularities, gaining a few percent of energy with each crossing. Among the accelerated particles are highly relativistic electrons, and those with energies ≳10 TeV will produce X-ray synchrotron radiation commonly observed in young SNRs (see Vink 2020 for a review). To reach those very high energies, the electrons need to reside close to the shock front, enabling fast repeated shock crossings. For this confinement close to the shock front, a highly turbulent magnetic field near the shock front is necessary.

Magnetic turbulence greatly affects the polarization of the light emitted. Synchrotron radiation from a nonthermal population of electrons with a power-law index of energy of 2–3 is intrinsically polarized at the 70%–75% level (see Equation (3).29 in Ginzburg & Syrovatskii 1965), but Cassiopeia A (Cas A) observations performed by the Imaging X-ray Polarimetry Explorer (IXPE; Weisskopf et al. 2022) showed that the degree polarization of the radiation in the 4–6 keV energy band is roughly 3% (Vink et al. 2022b), suggesting a highly turbulent magnetic field.

Despite the crucial need for high turbulence to achieve nonthermal X-ray emitting electrons and the recent X-ray polarization results, the most common models used to fit X-ray synchrotron spectra do not take into account turbulence effect

in shaping the resulting photon spectra. The synchrotron spectral shape emitted by a population of electrons having a power-law distribution with high-energy cutoff with particle index $\xi$ is, in the assumption of uniform magnetic field:

$$n(\hbar\omega) \propto (\hbar\omega)^{-\Gamma} \exp\left[ -\left( \frac{\hbar\omega}{\hbar\omega_c} \right)^{\beta} \right], \qquad (1)$$

where $\Gamma = (\xi + 1)/2$. In the loss-limited scenario adopted in Zirakashvili & Aharonian (2007), $\beta = 0.5$ while $\beta \approx 1$ in the `srcut` model available in XSPEC Reynolds & Keohane (1999). The latter has been the most commonly used to fit X-ray synchrotron-dominated spectra of SNRs (e.g., Bamba et al. 2005; Reynolds et al. 2008; Miceli et al. 2013), but recently X-ray SNR spectra were also analyzed using the relations from Zirakashvili & Aharonian (2007); see, e.g., Tsuji et al. (2021), Giuffrida et al. (2022), and Sapienza et al. (2022). In particular, Zirakashvili & Aharonian (2007) derived the analytical expression for the spectra of shock-accelerated electrons in the scenario in which the electron energy is loss-limited. They also recovered the nonthermal synchrotron spectra emitted by a population of such electrons. It is also common to describe the synchrotron emission with a simple power-law spectrum with the corresponding photon index $\Gamma \gtrsim 2.5$ (Bamba et al. 2005; Cassam-Chenaï et al. 2007; Helder et al. 2012). This is much steeper than the typical radio spectral index of SNRs of $\alpha \approx 0.5$, corresponding to the photon index $\Gamma = \alpha + 1 \approx 1.5$ or, for energies beyond the cooling break, $\Gamma_{cb} = \Gamma + 0.5 \approx 2$. This discrepancy has typically been explained by taking into account the curvature of the spectrum due to the cutoff expected in both age-limited (Reynolds & Keohane 1999) and loss-limited scenarios (Zirakashvili & Aharonian 2007). However, there are several
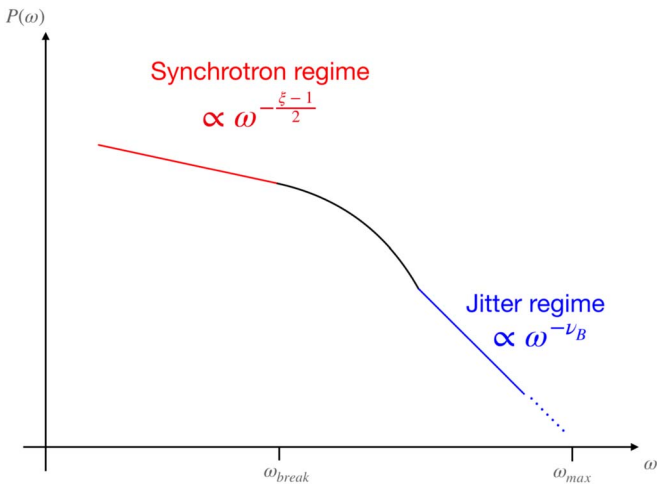
**Figure 1.** Radiation spectrum $P(\omega)$ produced by an ensemble of electron in a turbulent magnetic field (adapted from TF87). See also Reville & Kirk (2010; their Figures 5 and 6) for numerical results on the single particle emissivity. See the text for details.

detections of power-law spectra extending well beyond the soft X-ray band (i.e., $\gtrsim 10$ keV), at odds with the continuously steepening to be expected from a spectrum beyond the spectral cutoff.

The best example is provided by the SNR Cas A, a young (∼350 years old) and bright core-collapse SNR located at a distance of 3.4 kpc (Reed et al. 1995). Cas A shows a power law extending at least up to 50 keV in NuSTAR data (Grefenstette et al. 2015) and up to 100 keV according to RXTE data (Allen et al. 1997), BeppoSAX (Vink & Laming 2003), and more recent publications based on INTEGRAL and SWIFT (Renaud et al. 2006; Wang & Li 2016).

It is therefore natural to ask if a different mechanism, potentially linked to the often overlooked small-scale magnetic-field turbulence, might be responsible for this extended power-law component. The spectrum resulting from a motion of a relativistic electron in a highly nonuniform magnetic field was first investigated by Toptygin & Fleishman (1987, hereafter TF87) and, more recently, by Kelner et al. (2013, hereafter K13). The analytical results have also been numerically verified by Reville & Kirk (2010), but for the emissivity of a single particle. These authors refer to this radiation as *jitter radiation*. They show that an ensemble of relativistic electrons embedded in a highly turbulent magnetic field leads to a more sophisticated spectrum than the standard synchrotron one (see Figure 1, adapted from TF87).

Jitter radiation is sensitive to turbulence on length scales of

$$\lambda \ll 170(B/100\ \mu G)^{-1}\ \mathrm{km}, \tag{2}$$

with $B = 100\ \mu G$–$500\ \mu G$ being typical for the strengths reported for Cas A (Helder et al. 2012). These are scales much smaller than those usually considered for magnetic-field turbulence responsible for cosmic-ray acceleration ($\sim 10^{14}$–$10^{15}$ cm). The main factor limiting the magnetic turbulence at short scales is Landau damping, which is relevant at a scale $\lambda_{Ld} = \sqrt{\frac{T_e}{4\pi e^2 n_e}}$ with $T_e$ the electron temperature and $n_e$ the electron density. In order to make jitter radiation possible, it is then required that photon formation length $\lambda_{pf} \gg \lambda_{Ld}$.

Considering that a typical temperature of Cas A is 3 keV and an upstream density is $\approx 2$ cm$^{-3}$ (Hwang & Laming 2012), we obtain: $\lambda \gg \lambda_{Ld} \approx 0.15$ km.

From Figure 1 we can distinguish three main regimes: when the frequency $\omega$ is much lower than $\omega_{break}$, the radiation spectrum $P(\omega)$ is a power law with an exponential $\alpha = -\frac{\xi-1}{2}$, consistent with the prediction for the synchrotron radiation in a homogeneous magnetic field (e.g., Zirakashvili & Aharonian 2007); for $\omega \approx \omega_{break}$, $P(\omega)$ faces a decline, whose characteristics depend on the cutoff parameter $\beta$; for $\omega \gg \omega_{break}$, i.e., outside of this intermediate regime, $P(\omega)$ is, again, a straight power law, but here the exponential $\nu_B$ is the exponential of the magnetic-field turbulence spectrum. We do not focus here on the mathematical aspects of jitter radiation (the entire derivation can be found in TF87 and K13), but we just want to highlight the following: $\omega_{break}$ is the break frequency of the jitter radiation, related to the cutoff frequency $\omega_{cut}$ of standard synchrotron, i.e., with the electrons embedded in an homogeneous magnetic field, as $\omega_{break} = \omega_{cut} \times \frac{R_{L,j}}{\lambda}$ with $R_{L,j}$ the nonrelativistic Larmor radius; $\omega_{max} = \omega_{cut} \times (R_{L,j}/\lambda)^3$ is the maximum frequency to which the additional power law extends (K13).

In this paper, we analyzed Chandra/ACIS-S, NuSTAR/FPMA,B, INTEGRAL/ISGRI, and SWIFT/BAT data of Cas A, aiming at investigating the relative merits of the standard model, consisting of a synchrotron spectrum with exponential cutoff, versus its extension in the case of a highly turbulent magnetic field, the jitter radiation model. Interestingly, the jitter model can be used to estimate both the magnetic-field turbulence spectral index and the minimum length scale of magnetic-field turbulence.

The paper is organized as follows: in Section 2 we present all of the X-ray data considered, we describe their reduction and present results of image analysis; in Section 3 we show the results of the spectral analysis; in Section 4 we discuss the results and comment on their implications; and in Section 5 we wrap up the main findings and present our conclusion.

## 2. X-Ray Data Reduction and Regions Selection

We considered X-ray observations of Cas A in order to cover a wide X-ray energy range, from 0.5 keV up to roughly 100 keV. We analyzed data collected by Chandra/ACIS-S (operating in the 0.1–10 keV range; see Section 2.1; Garmire et al. 2003), NuSTAR (3–79 keV; see Section 2.2; Harrison et al. 2013), INTEGRAL/ISGRI (15 keV–1 MeV; see Section 2.3; Lebrun et al. 2003), and SWIFT/BAT (20–200 keV; Section 2.4; Barthelmy et al. 2005). All of the observations considered are listed in Table 1. Since INTEGRAL/ISGRI and SWIFT/BAT are coded masks and are not able to resolve Cas A, it was possible to perform spatially resolved spectral analysis only with Chandra and NuSTAR telescopes.

### 2.1. Chandra

We considered the Chandra/ACIS-S single observation of Cas A with highest exposure time (Obs ID 4638, PI Hwang). We reduced Chandra data with the task `chandra_repro` available within CIAO v4.14.0, with CALDB v4.9.7. We produced exposure-corrected images in the 0.5–8 keV and 4–6 keV energy bands with the task `fluximage`, displayed in the left panel of Figure 2 and, in red, in Figure 3, respectively.
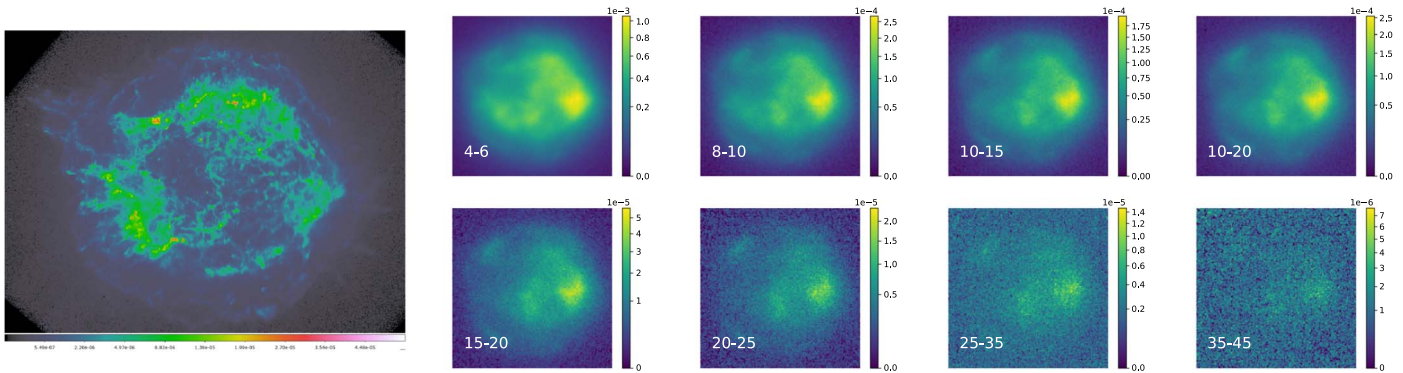
**Figure 2.** Chandra and NuSTAR exposure/vignetting-corrected images of Cas A. Leftmost panel: Chandra/ACIS-S count-rate image in the 0.5–8 keV band with a pixel size of $1''$ and a square root scale. Other panels: exposure/vignetting-corrected and mosaicked NuSTAR images of Cas A in various energy bands, reported on the images in units of keV, with a square root scale.

We used the task `specextract` to extract the spectra from the Chandra/ACIS-S event list with the proper RMF and ARF files. We selected different background regions in order to cross-check the consistency of our analysis, and we verified that the choice of the background did not influence our results.

### 2.2. NuSTAR

We analyzed 11 NuSTAR observations of Cas A, listed in Table 1, for a total exposure time of more than 2 Ms. The data have been reduced by using the `nupipeline` task available within NuSTARDAS, version 2.1.2. We set `SAAMODE=strict` and `TENTACLE=yes`, in order to be as conservative as possible with the background contamination. We produced exposure and vignetting-corrected count-rate images of Cas A in several energy bands, using the same ranges as in Grefenstette et al. (2015). We then mosaicked with `XIMAGE` the images in the same energy band obtained from separate observations and from the two different focal plane modules (FPM) detectors. The resulting mosaicked, and exposure- and vignetting-corrected images are shown, with the corresponding energy band, in Figure 2.

The images shown in the right panel of Figure 2 were deconvolved through the task `arestore`, based on the Lucy algorithm (Richardson 1972; Lucy 1974), in order to show that the morphology above 10 keV is consistent with the filamentary structure detected by Chandra. The comparison between the deconvolved NuSTAR (in green) and the Chandra (in red) images in the 4–6 keV band is shown in Figure 3. Indeed, the deconvolved NuSTAR count-rate image of Cas A in the 4–6 keV closely matched the same image observed by Chandra, proving the reliability of our region selection procedure. The main criterion for selecting the extraction regions was the high surface brightness both in the 4–6 keV and 10–20 keV bands, highlighted (in blue) in Figure 3. This is crucial, since high statistics over a wide energy range is required in order to robustly discriminate between spectra with and without cutoff, especially at energies higher than 10 keV. We highlight that, though the deconvolved NuSTAR image shows filamentary structures smaller than the region selected, we could not safely reduce the size of the extraction regions because of the NuSTAR point-spread function (PSF). Therefore, we extracted the NuSTAR spectra from the regions shown in Figure 3 through the task `nuproducts` following the recipe by Grefenstette et al. (2017).

### 2.3. INTEGRAL

Unlike Chandra and NuSTAR, INTEGRAL/ISGRI does not spatially resolve Cas A, and therefore no image analysis is possible. INTEGRAL's pointing strategy involves a dithering on a timescale of a few kiloseconds to reduce coded mask artifacts: each individual pointing is called a *science window*. We selected all 5686 science windows in which the spacecraft was pointing at less than $10°$ from Cas A. We built a catalog of the seven detected sources detected at more than $7\sigma$ in an 20–80 keV image obtained from 10% of the full sample, randomly selected. Using this catalog, we extracted the average spectrum of the source as seen by the IBIS/ISGRI detector (Lebrun et al. 2003) using version 11.2 of the Offline Science Analysis (Courvoisier et al. 2003) served through the Multi-Messenger Online Data Analysis[4] (Neronov et al. 2021). The resulting equivalent on-axis exposure is about 10.8 Ms over 17 Ms of observing time. We averaged spectra and responses through the mission: owing to the detector evolution and the relative source faintness, we could reliable use the data from 40–100 keV.

### 2.4. SWIFT

SWIFT/BAT is a coded mask detector that cannot spatially resolve Cas A. We used the spectra available at SWIFT/BAT_CasA,[5] and the response matrix was downloaded from SWIFT/BAT_RMF.[6] The total exposure time of the spectra is 180 Ms.

### 3. Spectral Analysis

We performed the spectral analysis with XSPEC (v12.12.1, Arnaud 1996) in several energy ranges and setups. We analyzed Chandra/ACIS-S data in the 4–6 keV band; NuSTAR/FPMA,B spectra in the ranges 4–5.5 keV, 9–15 keV, and 15–40 keV; INTEGRAL/ISGRI data in the range 40–100 keV; and SWIFT/BAT observations in the range 15–200 keV. All of the Chandra and NuSTAR spectra were optimally binned following the procedure described in Kaastra & Bleeker (2016) through the FTool task `ftgrouppha`. The corresponding background spectra were subtracted from Chandra/ACIS-S and NuSTAR/FPMA,B source spectra, whereas the

---

[4] https://www.astro.unige.ch/mmoda/
[5] https://swift.gsfc.nasa.gov/bat_survey/bs105mon/spectra/bat_index_1193.pha
[6] https://swift.gsfc.nasa.gov/bat_survey/bs105mon/data/swiftbat_survey_full.rsp
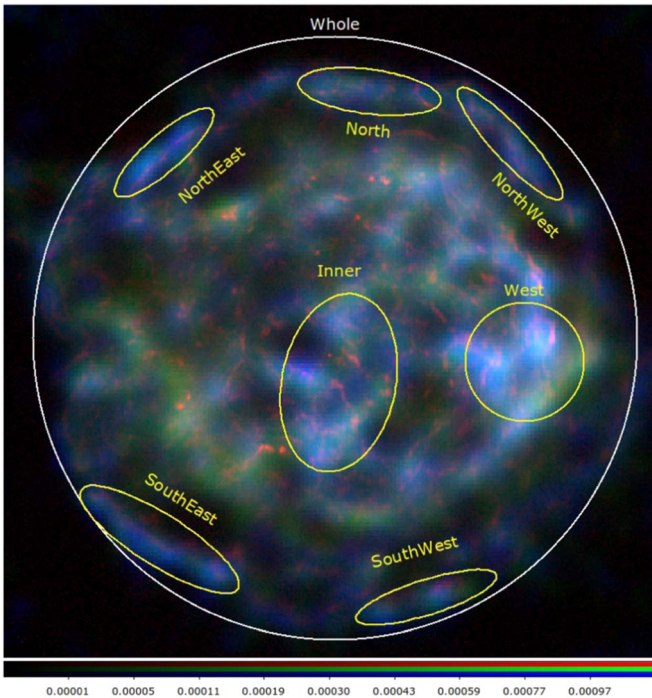
**Figure 3.** RGB Chandra and NuSTAR image of Cas A with a square root scale. In red, Chandra/ACIS-S count-rate image in the 4–6 keV band with a pixel size of 1″, in green the 4–6 keV NuSTAR deconvolved count-rate image, and in blue the 10–20 keV NuSTAR deconvolved image. The region used for the analysis of the whole remnant is shown in white, and the regions selected for the spatially resolved spectral analysis are shown in yellow.

**Table 1**
Observation Log Table

| Telescope | Obs ID | PI | Exposure (Ms) |
|---|---|---|---|
| Chandra | 4638 | Hwang | 0.164 |
| NuSTAR | 40001019002 | Harrison | 0.294 |
| | 40021002002 | Harrison | 0.288 |
| | 40021011002 | Harrison | 0.246 |
| | 40021012002 | Harrison | 0.239 |
| | 40021003003 | Harrison | 0.233 |
| | 40021001005 | Harrison | 0.228 |
| | 40021002008 | Harrison | 0.226 |
| | 40021001002 | Harrison | 0.190 |
| | 40021015003 | Harrison | 0.160 |
| | 40021002006 | Harrison | 0.159 |
| | 40021015002 | Harrison | 0.86 |
| | Total | | 2.3 |
| INTEGRAL | See Section 2.3 | | 10 |
| SWIFT | See Section 2.4 | | 180 |

energy bands; this is achievable only by considering wide spectral ranges.

This section is divided in various subsections, corresponding to the different regions of the SNR shown in Figure 3.

### 3.1. Whole Remnant

In this subsection we analyze the X-ray spectrum emitted by the "whole" Cas A and extracted from the white region shown in Figure 3. In this scenario, we can exploit the information collected by all of the telescopes considered in this project.

#### 3.1.1. Hard Band

We first focused on the hard energy band, >15 keV, where the X-ray thermal contribution is negligible and the total measured flux is ascribable to purely nonthermal emission processes. We only considered NuSTAR spectral bins where the background emission is a small fraction ($\lesssim$10%) of the Cas A emission, until an energy of 40 keV.

We performed the analysis either by fitting a single combined NuSTAR spectrum, obtained by processing the original NuSTAR spectra through the addascaspec task, and by simultaneously fitting the NuSTAR spectra extracted from the 11 observations. These two slightly different approaches have pros and cons that balance each other out. Summing the spectra leads to a single global spectrum with much higher statistics, smaller error bars and, therefore, to higher sensitivity to the spectral model adopted. However, since there were 11 separate NuSTAR observations performed in a time-lapse of 2 yr, the response matrix and the characteristics of the nonthermal emission might slightly change between the first and the last observations. On the other hand, the simultaneous analysis of the single spectrum extracted from each observation provided very reliable results, at the expense of the sensitivity to the spectral model.

We applied the spectral models introduced above to fit the X-ray synchrotron spectra of Cas A, each coupled to a component modeling the Galactic absorption (TBabs model in XSPEC) and to two Gaussians, accounting for the radioactive $^{44}$Ti lines observed in Cas A at 68 keV and 78 keV(e.g., Grefenstette et al. 2014). We also included a constant factor to

INTEGRAL/ISGRI and SWIFT/BAT spectra were already obtained with proper background subtraction. Our approach in analyzing the spectra is based on testing four different nonthermal scenarios: (i) a straight power law without any cutoff; (ii) an srcut model (Reynolds & Keohane 1999); (iii) a zira model (based on Zirakashvili & Aharonian 2007; see details in Appendix A); and (iv) a jitter model, which we incorporated in XSPEC (see details in Appendix A), representing the jitter scenario. In order to select the model that provides the best description of the data, we used three metrics: the standard $\chi^2$ statistic and its reduced version $\chi_r^2 = \chi^2/n$ with $n$ degrees of freedom; the Bayesian information criterion (BIC; Schwarz 1978), defined as BIC $=\chi^2 + m \ln(n)$, with $m$ being the number of free parameters in the model; and the Akaike information criterion (AIC; Akaike 1974), defined as AIC$=\chi^2 + 2m$. The model best describing the data is the one with the corresponding lower value of either $\chi_r^2$, AIC or BIC metrics.

As discussed in Section 1, the overall spectrum of jitter radiation can be divided in two components: the low-energy part, i.e., for $\omega < \omega_{\rm break}$, is similar in shape to the classical synchrotron component, and the high-energy part, i.e., for $\omega > \omega_{\rm break}$, which can extend up to $\gamma$-ray energies (K13). In the following, we will refer to the low-energy component as the *synchrotron component/regime*, to the high-energy component as the *jitter component/regime*, while we maintain the terms *synchrotron radiation* and *jitter radiation* when referring to the global radiation in the case of uniform and turbulent magnetic field, respectively. It is evident that in order to firmly detect jitter radiation we need to look for the absence of a cutoff in the spectra and a steepening of the photon index between two

**Table 2**
Best-fit Parameters for the 15–200 keV Band

|  | Parameter | Sim | Comb |
|---|---|---|---|
| zira | Norm[a] | $0.192 \pm 0.004$ | $0.191 \pm 0.04$ |
|  | $E_{cut}$ (keV) | $1.064^{+0.018}_{-0.017}$ | $1.08 \pm 0.02$ |
|  | $\chi^2$/d.o.f. | 2479/1869 | 317/120 |
|  | AIC | 2483 | 321 |
|  | BIC | 2494 | 327 |
| srcut | Norm[b] | $2180^{+90}_{-100}$ | $2140 \pm 0.80$ |
|  | Radio index | 0.77 (fixed) |  |
|  | $E_{break}$ (keV) | $1.07 \pm 0.03$ | $1.09 \pm 0.03$ |
|  | $\chi^2$/d.o.f. | 2349/1869 | 193/120 |
|  | AIC | 2353 | 197 |
|  | BIC | 2364 | 203 |
| pow | Norm[a] | $1.97 \pm 0.08$ | $1.94 \pm 0.08$ |
|  | $\Gamma$ | $3.336^{+0.016}_{-0.015}$ | $3.327 \pm 0.014$ |
|  | $\chi^2$/d.o.f. | 2270/1869 | 129/120 |
|  | AIC | 2274 | 133 |
|  | BIC | 2285 | 139 |

**Notes.**
[a] Units of photons/keV/cm$^2$ at 1 keV.
[b] Flux at 1 GHz in units of janskys. *Sim* and *Comb* mark the results obtained with the simultaneous analysis and with the combination of the NuSTAR spectra, respectively (see the text for details). The jitter model is not reported since it is indistinguishable from a simple power law.

take into account small variations on the extracted spectra due to PSF effects, cross-calibration (see Madsen et al. 2015), and to the temporal offset.

We left free to vary the following parameters for each nonthermal model: photon index $\Gamma$ and normalization for the power law; energy break $E_{break}$ and normalization for the srcut model, with the radio spectral index $\alpha$ fixed to 0.77 (Green 2019); and cutoff energy $E_{cut}$ and normalization for the zira model. For the jitter model, we left free to vary the photon indices $\Gamma_1$ and $\Gamma_2$, the normalization, the cutoff shape parameter $\beta$, and the energy break $E_{break}$, whereas the ratio between the normalization of the two components was kept fixed to 1. Values of reduced $\chi^2$ and best-fit parameters for each adopted model are shown in Table 2. Figure 4 shows the NuSTAR, INTEGRAL, and SWIFT spectra fitted with the different models and the corresponding residuals. The power-law model provided the best description of the spectra at a very significant ($>5\sigma$) confidence level, as can be clearly seen by the residuals in Figure 4 relative to the zira and cutoff models fitted on the combined spectra. The simultaneous analysis provided best-fit parameters perfectly consistent with those obtained with the combined spectra, guaranteeing the reliability of our results. The absence of any cutoff in such a wide (15–100 keV) energy range is the first hint of jitter radiation being a potentially important mechanism for the nonthermal X-ray emission from Cas A. If the turbulence length scale $\lambda$ is smaller than the gyroradius but larger than the photon formation length $\lambda_{pf}$, the slope of the spectrum is directly linked to the exponential of the magnetic-field distribution $\sigma_B$ (see K13) rather than to the turbulence spectrum. Given the purpose of this work, we will focus on the jitter scenario, i.e., assuming that $\lambda < \lambda_{pf}$. To investigate the jitter scenario, we fitted the same spectra with the jitter model, finding that the synchrotron component is unconstrained and that the jitter component has the same

characteristics as the simple power-law scenario, i.e., it is not possible to distinguish between a single power law and a jitter model. By interpreting the 15–100 keV emission as the *jitter component*, the synchrotron component must then be detectable at lower energies, outside this range[7]. Naturally, this is true not only for this hard energy range but for a generic X-ray spectrum. Given that the jitter component necessarily comes with a low-energy counterpart (the synchrotron component), the absence of a cutoff in the spectra simply reflects that the synchrotron regime is dominant at energies/frequencies lower than those considered. In this framework, the best-fit photon index of $\Gamma \sim 3.3$ implies a turbulence spectrum with an index $\nu_B = 2.3$, higher than typical values for Kolmogorov $\nu_{Kol} = 5/3$ and Kraichnan $\nu_{Kra} = 3/2$ turbulence. It is worth noticing that if $\lambda_{pf} < \lambda < R_{L,j}$, then $\Gamma \sim 3.3$ would imply $\sigma_B \sim 4.3$, from Equation (A5) in K13. Detailing the implications of this scenario is beyond the scope of this paper, and we leave it for future study. We will discuss possible explanations for this discrepancy in the jitter scenario in Section 4.2.

### 3.1.2. Soft Band

In Section 3.1.1 we focused on the hard ($\gtrsim 15$ keV) band of the spectra, finding hints for only one of the two components expected in the jitter radiation. If this component is actually the jitter component, we expect the synchrotron one to contribute at lower energies. The typical energy range in which soft X-ray nonthermal emission is studied in SNRs is between 4 and 6 keV, where there are no bright emission lines.[8]

We adopted the same methodology used for the hard energy band, i.e., we analyzed the Chandra and NuSTAR spectra in the 4–6 keV range with each of the different nonthermal emission models. We included an absorbing component (TBabs model in XSPEC), though its effect is minor at 4 keV. We kept the $N_H$ value fixed to $0.9 \times 10^{22}$, a value found from performing a fit of the Chandra 0.5–8 keV spectra. Given the narrow energy band, we did not consider the jitter model for the 4–6 keV range. The best-fit values with the corresponding errors bars (at the 90% confidence level) of $E_{break}$, $\Gamma$, and $E_{cut}$ are displayed in the rightmost set of points in Figure 5.

The best-fit values of $E_{break}$, $\Gamma$, and $E_{cut}$ show that the 4–6 keV NuSTAR and Chandra spectra are flatter than above 15 keV, where the nonthermal models adopted require higher values of $\Gamma$, $E_{break}$, and $E_{cut}$. While the steepening $\Delta\Gamma \approx 0.4$ is compatible with what we expect in the jitter framework, it is surprising to observe an increase of the break/cutoff energy with increasing energy range, challenging the picture predicting a unique cutoff for the spectrum of the "whole" Cas A, and in agreement with the results obtained in the 15–100 keV band.

### 3.2. Spatially Resolved Spectral Analysis

In Section 3.1 we showed the results of the analysis of the global X-ray spectrum of Cas A, providing us with information about the overall remnant. In order to investigate the spatial variation of the parameters characterizing the nonthermal

---

[7] The 100–200 keV band is covered only by SWIFT, and because of the wide error bars, only upper limits on the flux above 100 keV could be estimated (see Appendix C).
[8] Due to the poor spectral resolution of NuSTAR, some tail of the Fe K emission line contaminated the region between 5.5 and 6 keV. Therefore, we performed the NuSTAR spectral analysis between 4 and 5.5 keV.
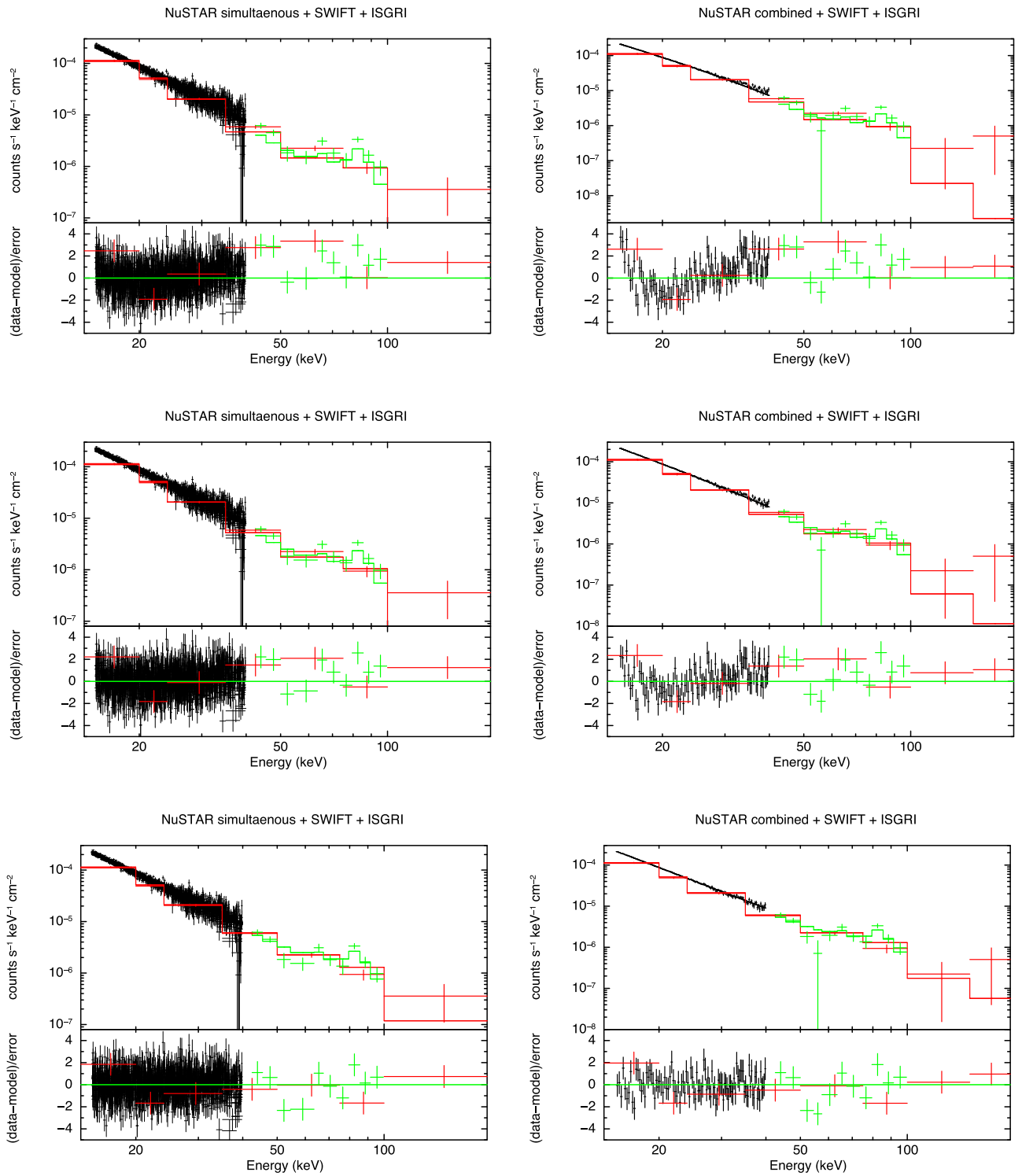
**Figure 4.** NuSTAR (black), INTEGRAL (green), and SWIFT (red) spectra of Cas A fitted with different models. The normalization of each spectrum is readjusted to the NuSTAR ones through the `setplot area` command available within XSPEC. The solid line represents the model. Panels from top to bottom: spectra are fitted with the `zira`, `srcut`, and `pow/jitter` model, respectively (the `jitter` model provides the same description as the pow). Left column panels: NuSTAR spectra from all of the observations are simultaneously fitted. All of the spectra are rebinned for graphical purposes. Right column panels: NuSTAR spectra from all of the observations are combined.

emission, we extracted Chandra and NuSTAR spectra[9] from the other seven regions shown in yellow in Figure 3. The main criterion for the region selection was the high surface

brightness both in the 4–6 keV and 10–20 keV that lead to us the identification of five regions close to the shock front: northwest (NW), north (N), northeast (NE), southeast (SE), and southwest (SW). Moreover, we also considered two additional regions, inner (I) and west (W): the former being characterized by particularly bright clumps at energies higher than 15 keV,
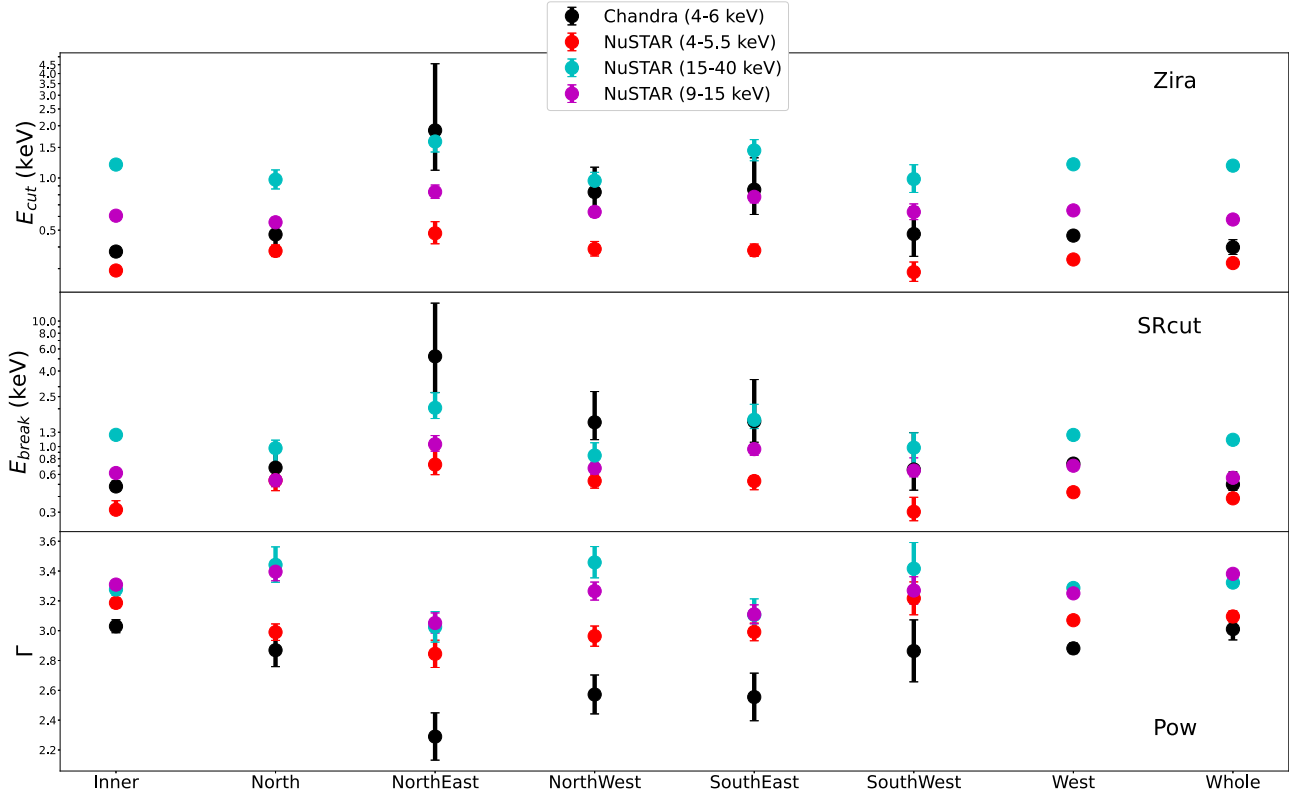
---

[9] SWIFT and INTEGRAL are not able to spatially resolve Cas A and cannot be used for this analysis.

**Figure 5.** Best-fit values of the nonthermal parameters in the `zira`, `srcut`, and power-law scenarios, as a function of the region and for different analysis setups. Error bars are estimated at the 90% confidence level. Each color represents the instrument used and the energy range considered: black for Chandra in the 4–6 keV band; red for NuSTAR data in the 4–5.5 keV band; purple for NuSTAR in the 9–15 keV band; and cyan for NuSTAR in the 15–40 keV band.

the latter corresponding to the location where the emission of nonthermal X-ray radiation indicates fast electron acceleration at the reverse shock (see, e.g., Orlando et al. 2022; Vink et al. 2022a).

We adopted the same procedure used for the whole remnant, by analyzing the Chandra and NuSTAR spectra in the 4–6 keV band and the NuSTAR spectra in the 9–15 and 15–40 keV bands. We here focus only on the spectra combined, in order to increase statistics particularly at energies above 20 keV. The best-fit parameters are shown in Figure 5, and the corresponding reduced $\chi^2$ values are shown in Figure 6.

The best-fit values of the nonthermal parameters (with the corresponding 90% confidence error bars) provide the following relevant information: (i) the cutoff energy measured with the `zira` model systematically increases with increasing energy; (ii) the break energy measured with the `srcut` model shows the same trend but less significantly than the `zira` scenario, with the NW region marginally consistent at a 90% confidence level with a fixed break energy; (iii) most of the regions are characterized by a steepening of the photon index; and (iv) independently of the spectral model adopted, the Chandra data systematically required flatter spectra than the NuSTAR spectra in the 4–6 keV energy band.

The average best-fit value of $E_{\text{break}}$ changed from 0.5 keV in the 4–6 keV energy band up to 1.5 keV at energies higher than 9 keV. A similar argument is valid also for $E_{\text{cut}}$, with an even higher discrepancy since the spectrum in the `zira` model falls off more quickly than in the `srcut` model. The fit performed by adopting the simple power-law model provided more accurate information on the steepening of the spectra across the
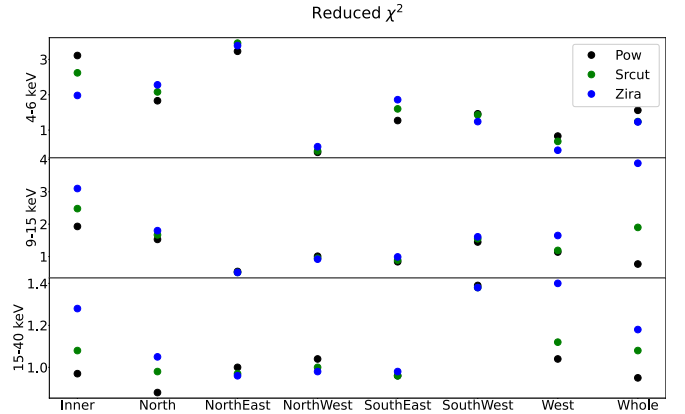


**Figure 6.** Values of $\chi^2_r$ for fits performed with different nonthermal models in the 4–6 keV, 9–15 keV, and 15–40 energy bands of the NuSTAR spectra. Black, green, and blue represent models with a power-law, `srcut`, and `zira` component, respectively.

SNR. Half of the regions (SE, SW, NE, and I) showed spectra with a constant photon index from 4 up to 40 keV, whereas the other half (NW, N, W, and the already discussed "whole" remnant) presented a clear steepening of $\Delta\Gamma \sim 0.4$.

We also measured a significant discrepancy between the best-fit values obtained from the Chandra and the NuSTAR spectra in the 4–6 keV energy band, with NuSTAR predicting steeper slope. We checked that this issue was not due to errors in the spectral extraction procedure (see Appendix B) and we

concluded that this is probably an effect of cross-calibration between the two telescopes. Given this inconsistency, we did not consider the Chandra spectra in the broadband 4–40 keV analysis presented in the following and we opted for a more conservative approach, based on the analysis of only the NuSTAR spectra.

Figure 6 shows the reduced $\chi^2$ for each of the model adopted as a function of the regions. Since all of the models adopted have the same number of free parameters, a direct comparison of the $chi^2$ values allowed us to identify the more appropriate model for each of the spectra. We found no significant preference for spectral models with or without cutoff in the 4–6 keV energy band. In regions N, NE, NW, SW, and W different nonthermal scenarios provided the same description already at a $1\sigma$ confidence level, with a $\Delta\chi^2 \leqslant 1$ among different models. Region SE was marginally better described by a straight power law, at a confidence level lower than 90% ($\Delta\chi^2 < 2.71$), and regions I and "whole" were described better by a cutoff at the 90% confidence level but not at $3\sigma$. Overall, these results indicated that it was not possible to robustly state whether the 4–6 keV emission was characterized by a cutoff or a straight power law. An additional source of uncertainty comes from the contribution of thermal continuum emission, which is neglected in our analysis and might contribute to the total flux, though this relative contribution could be as low as 5% as reported by Vink et al. (2022b), and it is in any case at least a factor of 3 lower than the nonthermal one (see Appendix D).

Similar points were also valid for the 9–15 keV and 15–40 keV bands. Regions N, NE, NW, SE, and SW were equally described by any of the spectral models adopted in both the energy bands. A fit with a power law provided a slightly better $\chi^2$ value in region W though not significant at more than 90% confidence. Only regions I and "whole" showed a significant preference for the power-law model both in the 9–15 and 15–40 keV energy bands, at odds with the 4–6 keV range. Overall, the results obtained from 15–40 keV band suggested an absence of cutoff in the spectra for regions I, N, W, and "whole," whereas the other regions did not permit discrimination between the three different adopted models.

The results of the spectral analysis presented so far could be summarized by three main points: (i) the $\chi^2$ values did not indicate a significant preference for either cutoff nor non-cutoff models. This is most likely due to the narrow energy bands considered: the spectral differences between a cutoff and a non-cutoff models are enhanced when looking at the evolution of the shape in wide energy bands. (ii) The best-fit values of the break/cutoff energies increased with energy, pointing against the presence of cutoff in the spectra. (iii) Best-fit values of photon indices indicated a steepening in at least half of the regions considered. In order to further investigate this point, we analyzed the curvature of the continuum between the soft (4–6 keV) and hard (15–40 keV) energy ranges (see Section 3.3).

## 3.3. Curvature of the Continuum

We investigated the change of the curvature of the NuSTAR spectra by extrapolating the best-fit nonthermal component measured from the 4–6 keV range in the 9–40 keV band: if the broadband nonthermal emission was characterized by a cutoff, then the best-fit model in the 4–6 keV band should well describe the data points in the 9–40 keV band as well. In

Figure 7 we show the results of this comparison for regions NW and SW, which were characterized by the two most extreme behaviors, with the best-fit values of the nonthermal parameters obtained from the 4–6 keV band analysis. The same plot for all of the regions is available in Appendix E.

Adoption of the `zira` model for the 4–6 keV energy range leads to a heavy underprediction of the higher-energy data points, indicating that this kind of cutoff was not suited to describe the broad nonthermal spectrum. The fact that the power law in the 4–6 keV band was systematically flatter than in the 9–40 keV was already clear in Figure 5. The only regions that did not show a clear steepening from the soft to hard X-rays were NW and SW (see Figure 7). Region SW was characterized by the highest $\Gamma \sim 3.2$ and showed the highest underprediction of the data 9–40 keV data points when considering cutoff models, suggesting that in this region the jitter component might be detectable already in the 4–6 keV band, while in other regions it might become so only at higher energies. The spectrum extracted from the NW presented the opposite behavior, being well described by the `srcut` model in the entire 4–40 keV range (see Figure 7), indicating that in this region, jitter radiation is not at work or that its synchrotron component is dominating the spectrum.

We also repeated this analysis by fitting the 15–40 keV data and extrapolating the obtained best-fit model down to 3 keV. As done in Figure 7 we here show the plots for the SW and NW regions (Figure 8), and we report the results for all of the regions in Appendix E.

The cutoff models, i.e., `zira` and `srcut`, systematically underpredicted the observed data points, with the best-fit value of $E_{\text{break}}$ and $E_{\text{cut}}$ higher than the corresponding values obtained from the 4–6 keV spectra only (as already observed in Figure 5). The region with the smallest variation in any of these parameter is NW, confirming that its emission is most likely dominated by synchrotron radiation. The extrapolation of the power-law model in the SW region lead to a significant overprediction of the data in the 4–6 keV band. It is worth mentioning that the results from the 15–40 keV are only indicative of and cannot be taken as firm proof of the presence or absence of steepening in the spectra, given that the wide error bars in this range lead to broad uncertainty on the slope of the high-energy tail, as in the case of region SW. In fact, while extrapolating the power law with $\Gamma = 3.4$ resulted in an overprediction of the 4–6 keV band, by taking $\Gamma = 3.2$, a value within the 90% confidence level, the resulting extrapolated power law very well described the 4–6 keV data points.

Overall, we found that the spectra face a steepening between the soft and the hard band and that the cutoff models describe the data systematically and significantly worse than the standard power law. However, the results presented so far did not take into account the shape of the spectrum in the two bands simultaneously. Therefore, we also fitted the 4–6 keV and 9–40 keV energy bands simultaneously (Section 3.4), excluding the 6-9 keV range that is dominated by the Fe K emission line.

## 3.4. Jitter Model

The results presented in Section 3.3 provided a qualitative estimate of the coherence of the continuum shape between the soft, 4–6 keV, and hard, 9–40 keV, energy bands. We fitted the 4–6 keV and 9–40 keV energy band for all of the regions with our `jitter` model (see Appendix A) and the standard `srcut`, `zira`, and `pow` models. We performed the analysis
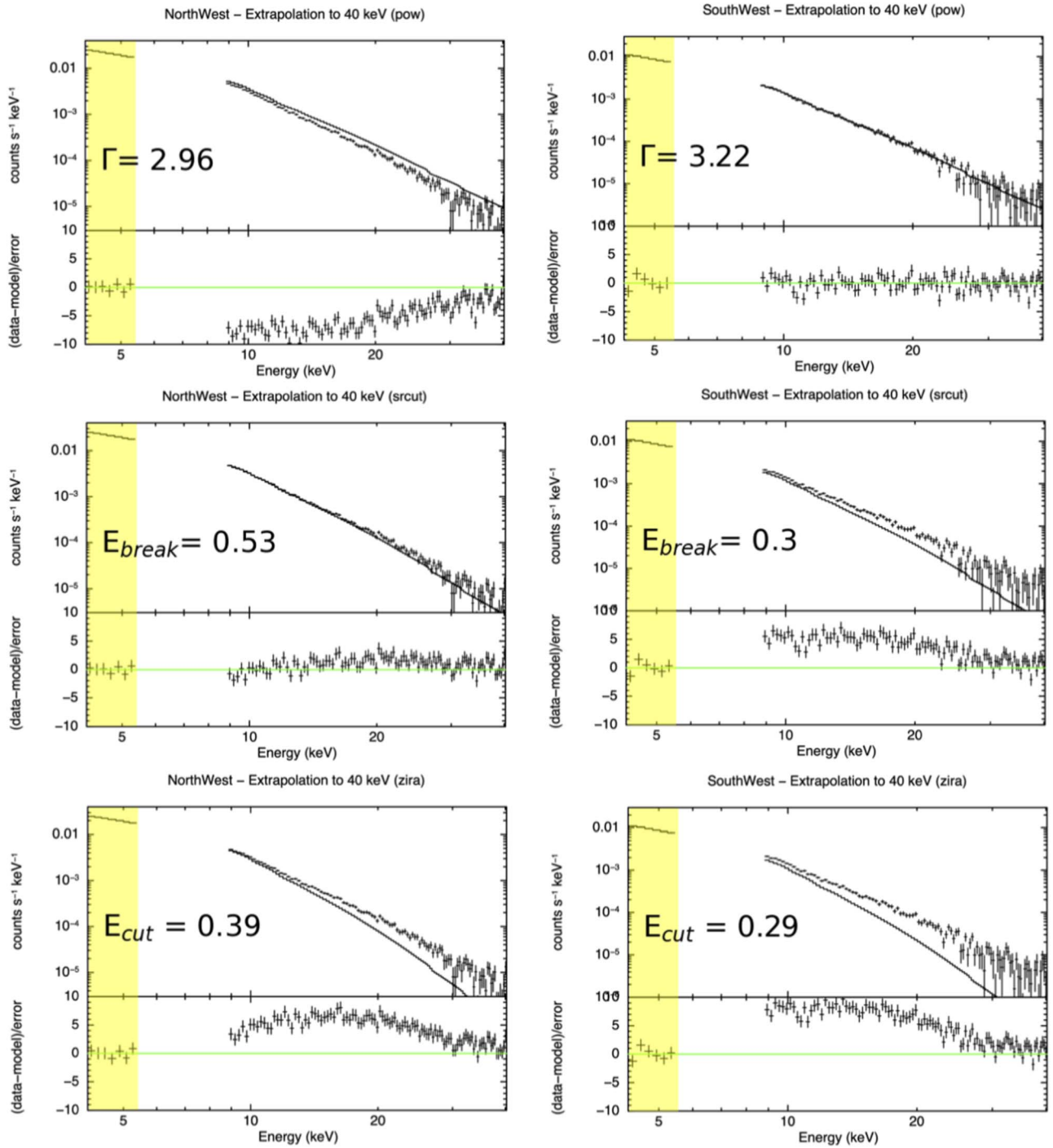
**Figure 7.** NuSTAR spectra in the 4–5.5 keV and 9–40 keV compared with the best-fit model (solid line) obtained by fitting only the 4–5.5 keV band for regions NW (on the left) and SW (on the right). The yellow area marks the spectral region in which the fit is performed. Each panel shows the 4–6 keV best-fit value of the nonthermal parameter considered: $\Gamma$, $E_{\mathrm{break}}$ (in keV units), and $E_{\mathrm{cut}}$ (in keV units) for the `pow`, `srcut`, and `zira` models, respectively.

either by leaving the $\beta$ parameter free to vary or by keeping it fixed to 0.5 (as in the `zira` model), 1 (as in the `srcut` model), or 2. We found that leaving $\beta$ free to vary significantly improved the quality of the fit for all of the regions but NW, with an average value of roughly 0.5 and systematically lower than 1. The best-fit parameters for all of the models with corresponding $\chi_r^2$, BIC, and AIC are listed in Table 3.

The recurrent striking feature evident in Table 3 is that the `jitter` model systematically provides a better description of the data than any cutoff model, as witnessed not only by the $\chi_r^2$ but also by the BIC and AIC metrics. While we were not able to pinpoint a favored model for the nonthermal emission for the 4–6keV and in the 15–40keV bands analyzed (see Figure 6), by simultaneously analyzing such wide spectral ranges, we are more sensitive to the emission pattern. Indications for this result were presented in Figure 5, where we noticed a (monotonic) increase in the photon index values and break energies with increasing energy ranges. We found values of $\Gamma_1$ slightly, but systematically, lower than those obtained with the analysis of the 4–6 keV band alone (red points in Figure 5).
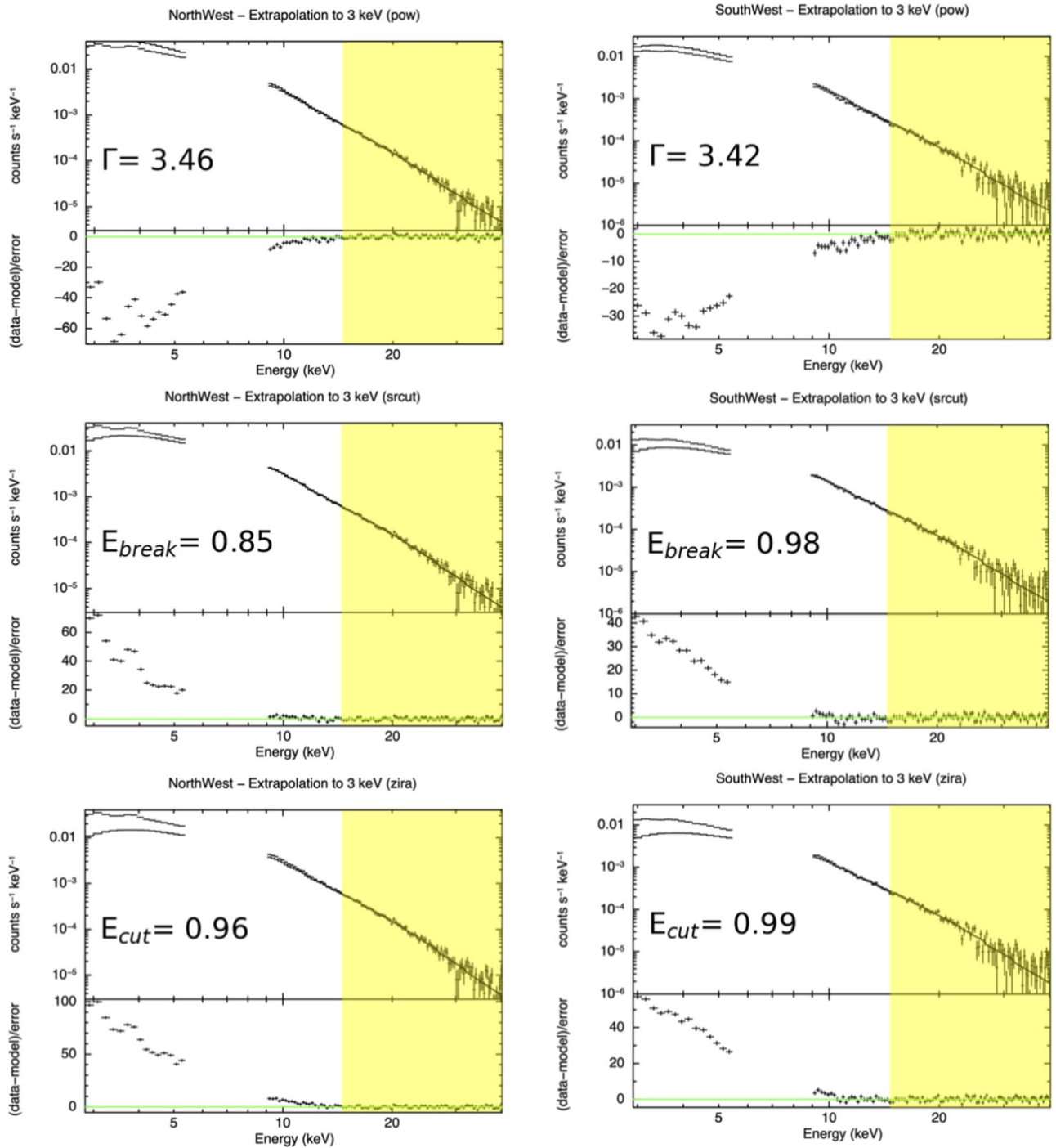
**Figure 8.** Same as Figure 7 but here the fit is performed in the 15–40 keV band and extrapolated down to 3 keV.

This is not surprising given that the `jitter` model provides the slope of the power law corrected by the effect of the cutoff, while a simple power law applied to a cutoff spectrum leads to an overall softer spectrum. On the other hand, best-fit values for $\Gamma_2$ were perfectly compatible with the $\Gamma$ best-fit values obtained from the analysis of the 15–40 keV spectra with the standard power-law model, since in this regime no curvature is present. Thanks to the simultaneous 4–6 keV and 9–40 keV analysis, we were now able to quantify and directly compare different models. We highlight this in Figure 9 where we show a comparison between the `srcut`, `zira`, and `jitter` models

for the NW, N, and SW regions, representing three different regimes.

All of the regions except for NW and SW showed indications of the presence of both synchrotron and jitter components of jitter radiation, as all of the parameters were satisfyingly constrained and the energy breaks lied within the spectral range investigated. Region N is shown in Figure 9 as clearly depicting this most common regime, with $4.5 < E_{\mathrm{break}} < 6$ keV, and an average value of roughly 5 keV. Region I was characterized by a slightly higher, but quite unconstrained, $E_{\mathrm{break}}$ value. In particular, it was compatible at a $3\sigma$ confidence level, with 5 keV, and could then be safely

**Table 3**
Best-fit Values on the 4–5.5 and 9–40 keV Bands

| Model | Parameter | Region | | | | | | | |
|---|---|---|---|---|---|---|---|---|---|
| | | Inner | North | Northeast | Northwest | Southeast | Southwest | West | Whole |
| TBabs | $N_{\rm H}$[a] | 1.7 | 1.1 | 1.0 | 1.13 | 1.5 | 1.4 | 2.0 | 0.9 |
| zira | $E_{\rm cut}$(keV) | $0.447^{+0.002}_{-0.002}$ | $0.421^{+0.004}_{-0.004}$ | $0.68^{+0.01}_{-0.01}$ | $0.51^{+0.006}_{-0.006}$ | $0.547^{+0.007}_{-0.007}$ | $0.488^{+0.009}_{-0.009}$ | $0.497^{+0.002}_{-0.002}$ | $0.494^{+0.001}_{-0.001}$ |
| | Norm[b] | $73.2^{+0.4}_{-0.4}$ | $8.5^{+0.1}_{-0.1}$ | $3.38^{+0.05}_{-0.05}$ | $6.03^{+0.08}_{-0.08}$ | $5.46^{+0.07}_{-0.07}$ | $2.9^{+0.06}_{-0.06}$ | $57.0^{+0.3}_{-0.2}$ | $599.0^{+2.0}_{-2.0}$ |
| | $\chi^2_r$ | 46.5 | 6.5 | 5.1 | 5.25 | 8.25 | 4.42 | 62.32 | 178.75 |
| | AIC | 5723.37 | 731.79 | 560.24 | 581.76 | 960.48 | 472.71 | 7918.88 | 25268.8 |
| | BIC | 5728.99 | 737.23 | 565.62 | 587.16 | 965.99 | 478.04 | 7924.57 | 25274.99 |
| srcut | $E_{\rm break}$(keV) | $0.462^{+0.004}_{-0.004}$ | $0.424^{+0.007}_{-0.007}$ | $0.9^{+0.02}_{-0.02}$ | $0.57^{+0.01}_{-0.01}$ | $0.65^{+0.01}_{-0.01}$ | $0.53^{+0.02}_{-0.02}$ | $0.545^{+0.003}_{-0.003}$ | $0.486^{+0.002}_{-0.002}$ |
| | Norm[c] | $930^{+10}_{-10}$ | $114^{+3}_{-3}$ | $28.0^{+0.8}_{-0.8}$ | $66^{+2}_{-2}$ | $55^{+1}_{-1}$ | $33^{+1}_{-1}$ | $650^{+5}_{-5}$ | $8050^{+60}_{-60}$ |
| | $\chi^2_r$ | 17.68 | 2.48 | 2.25 | 1.78 | 3.79 | 2.39 | 19.08 | 62.26 |
| | AIC | 2178.41 | 281.75 | 248.94 | 199.77 | 443.95 | 257.58 | 2427.71 | 8710.71 |
| | BIC | 2184.03 | 287.19 | 254.32 | 205.17 | 449.46 | 262.91 | 2433.4 | 8716.9 |
| pow | $\Gamma$ | $3.295^{+0.004}_{-0.004}$ | $3.333^{+0.009}_{-0.009}$ | $2.99^{+0.01}_{-0.01}$ | $3.186^{+0.009}_{-0.009}$ | $3.124^{+0.009}_{-0.009}$ | $3.22^{+0.01}_{-0.01}$ | $3.219^{+0.003}_{-0.003}$ | $3.347^{+0.002}_{-0.002}$ |
| | Norm[b] | $198^{+2}_{-2}$ | $22.8^{+0.4}_{-0.4}$ | $7.8^{+0.2}_{-0.2}$ | $15.2^{+0.3}_{-0.3}$ | $13.3^{+0.2}_{-0.2}$ | $7.5^{+0.2}_{-0.2}$ | $150.0^{+0.8}_{-0.8}$ | $2070^{+10}_{-10}$ |
| | $\chi^2_r$ | 1.5 | 2.28 | 1.05 | 1.83 | 1.11 | 1.38 | 2.75 | 2.14 |
| | AIC | 188.13 | 259.9 | 118.1 | 205.77 | 132.39 | 150.58 | 353.74 | 391.93 |
| | BIC | 193.75 | 265.34 | 123.48 | 211.17 | 137.9 | 155.91 | 359.43 | 398.12 |
| jitter | $\Gamma_1$ | $2.87^{+0.02}_{-0.3}$ | $2.87^{+0.02}_{-0.02}$ | $2.45^{+0.05}_{-0.05}$ | $3.0^{+0.08}_{-0.08}$ | $2.5^{+0.3}_{-0.3}$ | $2.9^{+0.2}_{-0.07}$ | $2.71^{+0.01}_{-0.01}$ | $2.724^{+0.006}_{-0.01}$ |
| | $E_{\rm break}$(keV) | $11.8^{+0.3}_{-0.3}$ | $5.2^{+0.1}_{-0.1}$ | $5.2^{+0.3}_{-0.1}$ | $40.4^{+0.5}_{-0.8}$ | $6^{+4}_{-2}$ | $4.4^{+0.2}_{-0.4}$ | $5.36^{+0.08}_{-0.03}$ | $4.59^{+0.04}_{-0.1}$ |
| | $\beta$ | $0.57^{+0.04}_{-0.04}$ | $0.38^{+0.03}_{-0.02}$ | $0.6^{+0.2}_{-0.2}$ | $1.2^{+0.7}_{-0.6}$ | $0.65^{+0.06}_{-0.06}$ | $0.3^{+0.1}_{-0.3}$ | $0.439^{+0.02}_{-0.003}$ | $0.485^{+0.007}_{-0.009}$ |
| | $\Gamma_2$ | $3.27^{+0.02}_{-0.02}$ | $3.429^{+0.02}_{-0.009}$ | $3.03^{+0.03}_{-0.02}$ | $2.6^{+0.5}_{-0.3}$ | $3.05^{+0.04}_{-0.03}$ | $3.5^{+0.1}_{-0.3}$ | $3.277^{+0.004}_{-0.008}$ | $3.359^{+0.004}_{-0.003}$ |
| | Norm[b] | $186^{+10}_{-10}$ | $29^{+2}_{-1}$ | $8.6^{+0.6}_{-0.4}$ | $12.2^{+0.8}_{-0.3}$ | $10.8^{+1.0}_{-0.9}$ | $12^{+4}_{-4}$ | $173^{+1}_{-2}$ | $2130^{+20}_{-20}$ |
| | $\chi^2_r$ | 1.19 | 1.06 | 0.95 | 1.03 | 0.93 | 1.38 | 1.14 | 1.04 |
| | AIC | 152.99 | 125.79 | 110.94 | 119.85 | 115.13 | 151.74 | 150.94 | 181.61 |
| | BIC | 166.93 | 139.25 | 124.26 | 133.21 | 128.77 | 164.91 | 165.04 | 196.99 |

**Notes.**
[a] Units of $10^{22}$ cm$^{-2}$, fixed in the fitting procedure.
[b] Units of $10^{-3}$ photons/keV/cm$^2$/s at 1 keV.
[c] Flux at 1 GHz in units of janskys.

included in this class of regions. Region NW showed an $E_{\rm break} \sim 40$ keV, at the upper edge of the spectral energy considered indicating that only the synchrotron component was detectable in the spectrum. This result nicely fits the picture discussed in Section 3.3 where the NW region was better described by the srcut model. Moreover, this is also the only region better reproduced by such a model rather than by a simple power law. Region SW showed a $\beta$ poorly constrained with an $E_{\rm break}$ of $\sim 4$ keV, in the bottom edge of the spectral range considered, indicating that in this region the synchrotron component of jitter radiation might be undetectable. Again, this feature was already suggested by the plot in Figure 5 where no clear steepening was observed between the 4–6 keV and 9–40 keV bands for the SW region. We also noticed that this was the only region that shows no preference for the jitter model with respect to a classical power law in terms of $\chi^2$, though the best-fit values of the two jitter photon indices differed significantly from the best fit found with the single power law. We investigated this discrepancy by imposing an energy break lower than 4 keV, representing a pure jitter component scenario. The resulting best-fit model showed a $\Delta\chi^2 = 2$, well within the 90% confidence range and a best-fit value for $\Gamma_2 = 3.2$, consistent with the results of the single power-law scenario. In conclusion, regions NW and SW represent two extreme possible regimes for jitter radiation, showing the absence of hard (jitter) and soft (synchrotron) components, respectively.

Since in the radio band a spectral index of $\sim 0.8$ is observed, we expected to measure $\Gamma_1 \sim 1.8$, or, by taking into account cooling break effects and the subsequent steepening, $\Delta\Gamma = 0.5$ (K13), $\Gamma_1 \sim 2.3$. Therefore, we repeated the analysis described above by setting priors on the upper limit of $\Gamma_1$, i.e., leaving $\Gamma_1$ free to vary but forcing it to be lower than 2.5, leaving some space for spatial variation of the radio index across Cas A. We found energy break values lower than 4 keV, i.e., outside of the X-ray domain considered, and we obtained an overall worse description of the spectra for all of the regions except for NE and SE. However, a significantly ($>3\sigma$) worse description was detected only for regions N ($\Delta\chi^2 \sim 30$), W ($\Delta\chi^2 \sim 70$), and "whole" ($\Delta\chi^2 \sim 200$). Overall, these results indicated that (i) in regions N, W, and "whole," some additional mechanism must be responsible for the radio-to-X-ray steepening of the synchrotron spectrum; (ii) in the other regions, the X-ray synchrotron spectrum is compatible (within $3\sigma$) with being the natural extrapolation of the radio one; and (iii) given the low value of $E_{\rm break}$ outside of the X-ray domain considered, the broadband 4–40 keV spectrum is dominated by the jitter component in all regions except for NE and SE. We will discuss this point in greater detail in Section 4.3.

## 4. Discussion

Here we report on a spectral analysis of the Chandra/ACIS-S, NuSTAR/FPMA,B, SWIFT/BAT, and INTEGRAL/ISGRI
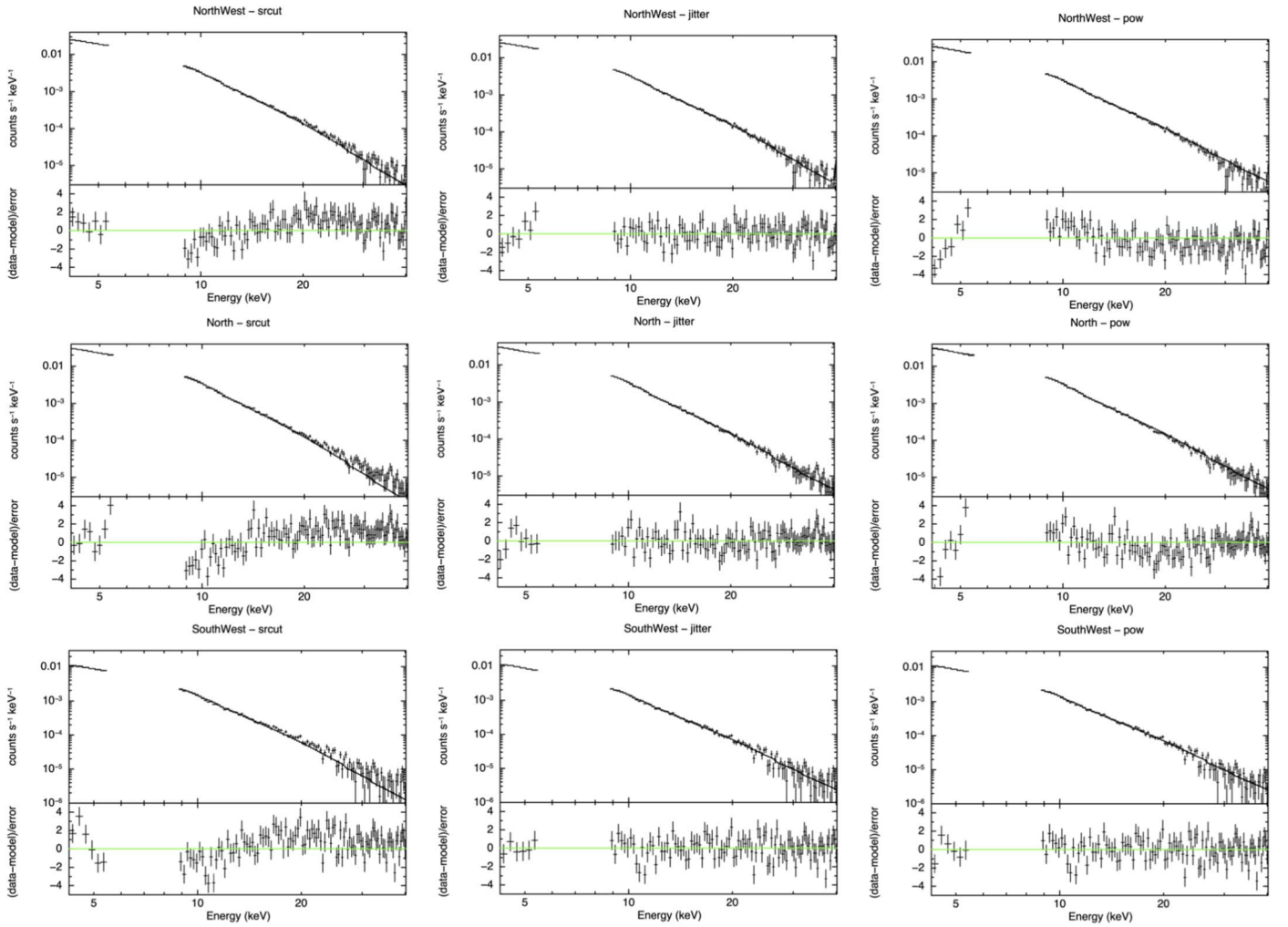
**Figure 9.** NuSTAR spectra from the NW (top line), N (central line), and SW (bottom line) regions fitted with the `srcut` (left column), `jitter` (central column), and `pow` (right column) models in 4–5.5 keV and 9–40 keV and with corresponding residuals.

data of the SNR Cas A, demonstrating that the nonthermal emission is better described by the jitter model than by a model of a power law with an exponential cutoff. In fact, in all regions but NW, the 9–40 keV spectra are not well fitted at all by a simple cutoff. The latter result was particularly evident for the "whole" remnant for which X-ray emission extends up to at least 100 keV, in disagreement with what we expect from a synchrotron regime beyond the cutoff. Additionally, there is supporting evidence at the $4\sigma$ level for nonthermal emission above 100 keV from CGRO/OSSE observations (The et al. 1996).

The absence of a cutoff in the hard X-ray spectra is indicative of the presence of a radiation mechanism different from the standard synchrotron radiation. The jitter radiation model provides a well-argued and physically motivated alternative radiation mechanism for the origin of the non-thermal hard X-ray radiation. The photon spectrum of jitter radiation self-consistently takes into account the effect of the magnetic-field turbulence and directly connects it to the shape of the hard X-ray emission. In contrast, the standard model of a power-law spectrum with some form of exponential cutoff assumes a homogeneous magnetic field, whereas, paradoxically, the high cutoff energy itself requires a highly turbulent magnetic field. In the following sections, we discuss in detail the implication of these results on the turbulent magnetic field in which the electrons are embedded.

### 4.1. Synchrotron versus Jitter Regimes

The jitter radiation model (TF87, K13) is an extension of synchrotron radiation in presence of a highly turbulent magnetic field. For synchrotron radiation, the acceleration is perpendicular to the magnetic field, causing the electrons to follow a helical path, with the magnetic field assumed to be constant at length scales comparable to the gyroradius of the electrons. Jitter radiation is a consequence of magnetic-field fluctuations on scales smaller than the photon formation length, causing deviations from the regular, helical path.

At frequencies below $\omega_{\mathrm{break}}$, jitter radiation simply reduces to classical synchrotron radiation, which dominates the radiative spectrum from the populations of relativistic electrons. If the electron energy distribution is a power law in energy—$n(E) \propto E^{-\xi}$, then the synchrotron radio spectral index is $\alpha = (\xi - 1)/2$, translating into a photon index $\Gamma = \alpha + 1$. For Cas A, $\alpha = 0.77$ and $\Gamma = 1.77$, although a flattening of the average radio-to-infrared nonthermal spectrum is likely happening above 10 GHz (see the discussion in Domček et al. 2021).

At the shock front, the electron distribution is expected to have an exponential cutoff, caused by the fact that energy gains due to DSA are at high energies limited by radiative losses—in the so-called loss-limited scenario—or alternatively by a limited time available for acceleration, the time-limited

scenario (Reynolds 1996; Helder et al. 2012). Farther downstream of the shock, the maximum energy of electrons is lower, as after having participated in the DSA process, electrons keep losing energy. Given the limited lifetime of an SNR, there is a maximum energy for the electrons that were accelerated at the beginning. This gives rise to a break—the cooling, or age break —in the synchrotron spectrum with steepening of $\Delta\alpha = \Delta\Gamma = 0.5$ (e.g., Longair 2011). For Cas A, the spectrum beyond the cooling break is expected to have an index $\alpha \approx 1.1$ —1.3, or $\Gamma = 2.1$–2.3. This is clearly flatter than the power law of the hard X-ray radiation, which is closer to $\Gamma \approx 3$ (see Table 3). Moreover, the nonthermal X-ray emission is clearly associated with narrow filaments at the shock front (Vink & Laming 2003) for which we expect the synchrotron spectrum to have an exponential cutoff, rather than a broken power law. The cutoff photon energy and the cutoff electron energy are related by the following:

$$\hbar\omega_{cut} \approx 0.19(B/100~\mu G)(E_{e,cut}/10~\text{TeV})^2~\text{keV},\qquad(3)$$

supporting the idea of a cutoff photon energy in the range of 0.2–10 keV, given the uncertainty in $B$ and $E_{e,cut}$.

Based on the X-ray synchrotron model of the filaments, the measured photon cutoff energy corresponds to an electron cutoff energy of around 10 TeV (Vink & Laming 2003). This is also in agreement with the cutoff energy inferred from the very-high-energy gamma-ray emission measured by MAGIC (Ahnen et al. 2017). However, surprisingly, the cutoff inferred from the gamma-ray spectrum pertains to the hadronic (proton) cosmic-ray cutoff, rather than the electron cutoff energy. Clearly the lack of a clear cutoff energy in the hard X-ray spectra, the steepness of the spectra, and the generally good fits provided by the `jitter` model lend support to the hypothesis that both the synchrotron and jitter components are contributing to the nonthermal X-ray emission from Cas A. An exceptional case is provided by the spectrum from the NW, where the `jitter` model suggests an unusually high break energy of $E_{break} \sim 40$ keV, compared to 4–5 keV elsewhere.

### 4.2. Magnetic-field Turbulence Spectrum and Length Scales

In this Section we take advantage of the results of the spectral analysis to infer significant information on the turbulence energy distribution and spatial scale. Magnetic-field turbulence is an integral part of both collisionless shock heating and particle acceleration through the DSA mechanism. For DSA, magnetic-field turbulence is needed at the scales of the Larmor radius. For the highest-energy electrons, this corresponds to $R_L = E_e/eB \approx 3 \times 10^{14}(E/10~\text{TeV})(B/100~\mu G)^{-1}$ cm. This is much larger than the turbulence length scales relevant for jitter radiation, which are below the non- or mildly relativistic Larmor radius, $R_{L,j} \equiv m_e c^2/eB = 170(B/100~\mu G)$ km (K13). This scale is therefore not so much relevant for the acceleration of relativistic particles through DSA, but it is for the plasma heating of collisionless shocks (and for the initial stages of particle acceleration), taking place on the ion inertial length scale, $\lambda_{ii} = c/\omega_{pi} \approx 230 n_p^{-1/2}$ km.

For synchrotron radiation, the photon index $\Gamma_1 = \frac{\xi+1}{2}$ reflects the spectral index $\xi$ of the electron spectrum. In contrast, in the jitter regime $\Gamma_2$ reflects the spectral index $\nu_B$ of the magnetic-field fluctuation spectrum (defined as in Equation (69) of K13, with the relation $\Gamma_2 = \nu_B + 1$. The spectral indices reported here (Table 3) range from $\Gamma_2 = 3$ (NE) to 3.4 (N),

**Table 4**
Upper Limits on the Minimum Turbulence Scale and Particles' Cutoff Energy

| Region | $E_{break}$ (keV) | $E_{max}$ (LL) (keV) | $\lambda/B_{100}$ (UL) (km) | $E_{ph,cut}$(UL) (keV) | $E_{e,cut}B_{100}^{-1/2}$ (UL) (TeV) |
|---|---|---|---|---|---|
| Inner | 4.5 | 40 | 57 | 1.5 | 15 |
| North | 5.2 | 40 | 61 | 1.9 | 17 |
| Northeast | 5.2 | 40 | 61 | 1.9 | 17 |
| Northwest | 40.4 | 40 | 171 | 41 | 78 |
| Southeast | 6.0 | 40 | 66 | 2.3 | 19 |
| Southwest | 4.4 | 40 | 56 | 1.5 | 15 |
| West | 4.7 | 40 | 59 | 1.6 | 16 |
| Whole | 4.5 | 100 | 36 | 0.9 | 12 |

**Note.** Scaled by $B_{100} = B/100~\mu G$. "LL" and "UL" stand for lower and upper limit, respectively.

implying $\nu_B \approx 2.0$–2.5. Models of magnetic-field fluctuation spectra that are often considered are $\nu_B = 5/3$ for Kolmogorov turbulence (Kolmogorov 1941) and $\nu_B = 3/2$ for Kraichnan turbulence (Kraichnan 1965). Both are flatter than what is implied by the jitter model. However, Kolmogorov and Kraichnan turbulences assume injection of large-scale turbulence at a large length scale cascading down to smaller length scales. At shock fronts, the generation of turbulence is different. For example, Takabe (2023) argued that the Weibel instability results in a saturated spectrum with $\nu_B = 2$. This would correspond to $\Gamma_2 = 3$, compatible with what we found here, and in line with the hard X-ray spectra of other young SNRs, which are also generally around $\Gamma = 3$ (e.g., for SN1006; Li et al. 2018).

For synchrotron radiation, the cutoff photon energy relates to the highest electron energy; see Equation (3). For jitter radiation, the maximum photon energy $E_{max}$ is (K13)

$$E_{max} \sim (R_{L,j}/\lambda)^3 \hbar\omega_{cut} \Rightarrow \lambda/R_{L,j} = \sqrt{E_{break}/E_{max}},\qquad(4)$$

for which we take advantage of the relation (K13)

$$E_{break} \sim \hbar\omega_{cut} \frac{R_{L,j}}{\lambda},\qquad(5)$$

with $\lambda$ the turbulence scale and

$$\omega_{cut} = \frac{3}{2}\frac{eB}{mc}\left(\frac{E_{e,cut}}{mc^2}\right)^2\qquad(6)$$

being the cutoff frequency of the standard synchrotron regime (i.e., when $R_{L,j} << \lambda$), with $B$ being the average magnetic field.

From Equation (6) we can resolve with respect to the cutoff energy of the population of electrons $E_{e,cut}$ emitting jitter radiation obtaining:

$$E_{e,cut} = \sqrt{\frac{2}{3}\frac{\omega_{cut}m^3c^5}{eB}} = \sqrt{\frac{2}{3}\frac{m^3c^5}{eB}\frac{E_{break}\lambda}{\hbar R_{L,j}}}.\qquad(7)$$

All of the quantities in Equation (7) are known, though we only have an upper limit on $\lambda$, and we then could put only upper limits on the particles' cutoff energy as well. The resulting values are shown in Table 4.

For Cas A, the downstream magnetic-field strength has been estimated to be in the range of 100–500 $\mu G$ (Vink & Laming 2003; Berezhko & Völk 2004; Helder et al. 2012). For that reason, we normalize to $B_{100} \equiv B = 100~\mu G$, so that we

can translate the best-fit values of $E_{break}$ and our lower limits for $E_{max}$ into an *upper limit* on the minimum scale for the magnetic-field fluctuation length scale, $\lambda_{min}$, as shown in Table 4. For calculating $E_{e,cut}$, we included an additional factor of 2/3 in Equation (3), as suggested by K13.

The table shows that the condition of Equation (2) required for jitter to be at work is satisfied for all of the regions except the NW, indicating that magnetic-field fluctuations must be present to scales of ~100 km and smaller. Such values are remarkably small, and at a scale barely probed by in situ measurements of interplanetary shocks, which measure magnetic-field fluctuations with a resolution of seconds to minutes, which translates into length scales of 100–6000 km, for plasma speeds of $100\ km\ s^{-1}$. Noticeably, the cutoff energy of the particles in the jitter scenario does not differ much from the standard synchrotron, which predicts $E_{e,cut} \sim 10\ TeV$.

### 4.3. Polarization and Filaments' Width

If the nonthermal hard X-ray emission from Cas A and other young SNRs is indeed due to jitter radiation, then we need to rethink some of the phenomenology of nonthermal X-ray emission that is often taken for granted. In particular, there are two aspects for which jitter radiation may have important consequences: X-ray polarization, and the widths of X-ray synchrotron filaments.

So far, two X-ray polarization measurements by IXPE of young SNRs have been reported, for Cas A (Vink et al. 2022b) and Tycho's SNR (Ferrazzoli et al. 2023). For Tycho's SNR, the X-ray rim was reported to have 9% polarized X-ray emission, whereas for Cas A, the polarization fraction was even lower: no isolated regions with a large polarization fraction could be found, and the overall polarization fraction on the nonthermal emission must be below 4%, with a polarization angle topology consistent with radially aligned magnetic fields. Again, this argues for highly turbulent magnetic fields at scales $\lesssim 10^{17}\ cm$ in the context of synchrotron radiation. However, it is surprising that there is not a large-scale anisotropy in the magnetic field, due to plasma shear—incurring radially oriented magnetic fields—or to shock compression causing tangential magnetic fields. Since jitter radiation is sensitive to very-small-scale magnetic-field fluctuations, which are largely isotropic, it should not be intrinsically polarized.[10] In the context of Cas A (and to a lesser extent Tycho's SNR), the low X-ray polarization fraction is simply a feature of jitter radiation. The small residual X-ray polarization suggests that a fraction of the nonthermal radiation is ascribable to the synchrotron regime, and hence the synchrotron cutoff energy $E_{ph,cut}$ should be in the soft X-ray band, as indeed seems to be the case according to Table 3. A consequence that is potentially measurable should be that at larger photon energies—i.e., moving away from the synchrotron part of the spectrum—the polarization fraction should decrease. This is opposite to what is expected for pure synchrotron radiation, where at higher energies the spectrum steepens and originates from smaller regions, giving rise to a polarization fraction increasing with energy (see Bykov et al. 2011).

As for the narrow width of the nonthermal X-ray filaments, these are usually interpreted as due to strong synchrotron losses

of the high-energy electrons, giving rise to a width of $l_{syn} = \frac{1}{4} V_s \tau_{syn}$, with $V_s$ being the shock velocity and $\tau_{syn} \approx 624/B^2 E_e$ s, the synchrotron loss timescale, or they are thought to be indicative of the electron diffusion length scale, $l_{diff} \approx 4D_2/V_s$, with $D_2 = \eta c E/eB$ the diffusion coefficient and $\eta = 1$ in the Bohm limit. We see that for $l_{syn}$, the synchrotron filaments' widths should decrease with electron energy, and increase for $l_{diff}$. However, near the cutoff electron energy, one expects $l_{syn} \approx l_{diff}$ (e.g., Vink 2020).

Nevertheless, there have been attempts to measure the filament widths as a function of photon energy. Most recently this was done by Picquenot et al. (2023), who reported that there is a "narrowing with energy of the synchrotron filaments in Cassiopeia A," and that the energy dependency of this narrowing seems stronger at high energy (Picquenot et al. 2023). In light of the synchrotron model, this is somewhat surprising, as it suggest that filaments' widths are purely defined by $l_{syn}$ and not $l_{diff}$. However, these measurements can be explained by jitter radiation, considering that the small-scale magnetic-field fluctuations generated near the shock dampen farther downstream of the shock. This argument is somewhat reminiscent of the work of Pohl et al. (2005); however, that work argued for a decay of the overall magnetic field, rather than a decay of the magnetic-field turbulence. So jitter radiation offers a natural explanation for the narrowing of the filament widths with energies. In the context of Cas A, it would imply again that at softer X-ray energies the width is partially determined by the combination of $l_{diff}$ and $l_{syn}$, but at higher energies, where the spectrum becomes more dominated by the jitter component, the width starts to be determined by the length scale over which small-scale turbulence is dampened. In principle this suggest that the narrowing of the filaments should only become prominent for energies beyond $E_{break}$, consistent with the findings of Picquenot et al. (2023).

### 5. Summary and Conclusions

In this paper, we presented our results on the analysis of multi-instrument X-ray data of the SNR Cas A, aiming at characterizing the shape of nonthermal emission in a wide energy band and in investigating its origin. We analyzed Chandra/ACIS-S, NuSTAR/FPMA,B, SWIFT/BAT, and INTEGRAL/ISGRI observations of Cas A in the 4–100 keV energy band and performed a spatially resolved spectral analysis adopting various nonthermal spectral models. Our findings can be summarized as follows:

1. While DSA intrinsically requires high magnetic turbulence, the spectral models used to fit nonthermal spectra of SNRs do not include the effect of turbulence in the shaping of the spectra. The standard approach to fit SNR spectra in the 4–6 keV energy band to investigate its synchrotron radiation is insensitive to the actual shape of the nonthermal model adopted.

2. The 15–100 keV spectra of the "whole" Cas A can be adequately fitted only through a power law with a photon index $\Gamma \sim 3.3$. The 15–100 keV spectra are not well fitted either by the `srcut` (Reynolds & Keohane 1999) or the `zira` (Zirakashvili & Aharonian 2007) model, as there is no evidence for an exponential cutoff.

3. A jitter model describes the 4–40 keV spectra of all of the regions considered much better than any other model,

---

[10] Private communication Brian Reville. Note that Prosekin et al. (2016) calculated the expected polarization of jitter radiation, but assumed only two-dimensional fluctuations, showing that an anisotropic turbulence could still lead to a considerable amount of polarized light.

showing a clear steepening of the spectrum incompatible with a cutoff and with a best-fit photon index $\Gamma_2 \sim 3$–3.4.

4. The best-fit photon index $\Gamma_2 \sim 3$–3.4 implies a spectral index for the turbulence spectrum $\nu_B \sim 2$–2.4, higher than common values such as Kolmogorov $\nu_{\text{Kol}} = 5/3$ and Kraichnan $\nu_{\text{Kra}} = 3/2$. This applies to magnetic-field fluctuations on scales of $\sim100$ km, much smaller than the scales normally invoked for the DSA mechanism, and more in line with fluctuations near collionless shocks as induced by the Weibel instability.

5. We estimated upper limits on the minimum turbulence scale that are typically smaller than 100 km, whereas the estimated transition energies from synchrotron to jitter regimes imply cutoff electron energies of typically 15 TeV, as in the standard synchrotron scenario.

6. If indeed the nonthermal X-ray emission is due to both synchrotron and jitter components, this offers an alternative natural explanation for the low polarization fraction for Cas A and the narrowing of nonthermal X-ray filaments with increasing energy. So, potentially, with nonthermal X-ray emission, we are zooming into regions very close to the collisionless shocks themselves.

### Appendix A
### Zira and Jitter Models in XSPEC

#### A.1. Zira

We implemented Equation (37) of Zirakashvili & Aharonian (2007) through the mdefine task available within XSPEC, defining a new zira model. The corresponding equation in the notation used in this paper can be read as

$$(E_{\text{rad}}/E)^2 (1 + 0.38\sqrt{E/E_{\text{cut}}})^{11/4} \exp[-(E/E_{\text{cut}})^{1/2}] \quad \text{(A1)}$$

where $E_{\text{rad}}$ is always kept fixed to 1. The exponent "2" in $(E_{\text{rad}}/E)^2$ is added to match the default XSPEC units.

#### A.2. Jitter

The total jitter model does not have an analytical expression and cannot be included within XSPEC through the mdefine task. We followed the approach described in Load_model_XSPEC to include our jitter model in the library of the available models. The synchrotron-dominated and jitter-dominated regimes are, respectively, modeled by two power laws with an additional exponential cutoff for the low-energy component. However, the simple addition of both components in a single model does not replicate the complex shape of the total emission, and advocates for additional energy- and/or flux-dependent constraints. For this purpose, the flux given by the two components is computed iteratively in each energy bin (starting from low energy), and the highest is kept as the model flux. The ratio of both component fluxes, labeled jratio, is added as a parameter to the model and acts as a normalization.

For continuity and self-consistency reasons, the jitter flux is set to zero for energies lower than the synchrotron break, preventing any ill behavior in situations of steeper jitter slope, resulting in high flux at low energies. We tested our model by comparing it with other well-known models such as pow, bknpower (i.e., a broken power law), and cutoffpl (a power law with an exponential cutoff), in regimes in which the jitter radiation simply reduces to one of these.

The jitter model is finally described by six parameters as follows: PhoIndex1: synchrotron power-law slope ($\Gamma_1$), Ebreak1: synchrotron break energy ($E_{\text{break}} = \hbar\omega_{\text{break}}$, with $\omega_{\text{break}}$ defined in Figure 1), PhoIndex2: jitter-radiation power-law slope ($\Gamma_2$), jratio: ratio between flux in regime 1 and regime 2 ($P_2/P_1$ in TF87), beta1: shape of the exponential cutoff around Ebreak1 ($\propto \exp[-(\omega/\omega_{\text{break}})^\beta]$), and norm: total normalization of the model.

### Appendix B
### Cross-calibration between X-Ray Telescopes

We investigated potential issues causing the significant discrepancy observed in the Chandra and NuSTAR spectra in the 4–6 keV energy range. The distortion in the Chandra/ACIS-S spectra could be produced by pileup effects. We produced, through the pileup_map task within *CIAO*, a pileup map of Cas A, finding that the average pileup fraction in the regions considered is roughly 3%, and it was therefore excluded as a possible origin for the flattening. We checked that the flux of NuSTAR spectra in the >15 keV energy band are consistent with those reported for BeppoSAX (Vink & Laming 2003) and INTEGRAL (Renaud et al. 2006) considering the nominal cross-calibration constant (Madsen et al. 2015, 2022). We used srcflux on the Chandra image in the 4–6 keV band and checked that the observed counts matched the counts in the same energy range in the spectra. We also repeated this procedure for the NuSTAR data with the ftool countsinregion. Finally, we used adopted different values for the parameter boxsize = 5, 10, 20, 30, and 40 obtaining identical spectra and set flatflagarf=yes, as in Grefenstette et al. (2017).

### Appendix C
### SWIFT Upper Limit on Flux

We estimated the upper limit on the X-ray flux of A Cas above 100 keV by estimating, through the error command within XSPEC, the 90% and 99.7% confidence level (corresponding to $\Delta\chi = 2.706$ and $\Delta\chi^2 = 9$) starting from the SWIFT/BAT spectra of Cas A. The best-fit model was a power law having $\Gamma = 3.5$. The error on the flux was estimated through the cflux component. The Gaussian components, describing the lines of Ti44, are kept fixed since these are not resolved by SWIFT but contribute to the global flux. The corresponding upper limits on the flux between 100 and 200 keV were $0.28 \times 10^{-11}$ erg/s and $0.33 \times 10^{-11}$ erg/s at the 90% and 99.7% confidence levels, respectively.

### Appendix D
### Nonthermal to Total Flux Ratio

In Section 3.2 we showed that we cannot rule out or confirm the presence of a cutoff in the 4–6 keV spectra. As already mentioned, a possible source of uncertainty is the thermal emission from the shocked-heated plasma. Because of the bad spatial resolution of NuSTAR and the need for high statistics
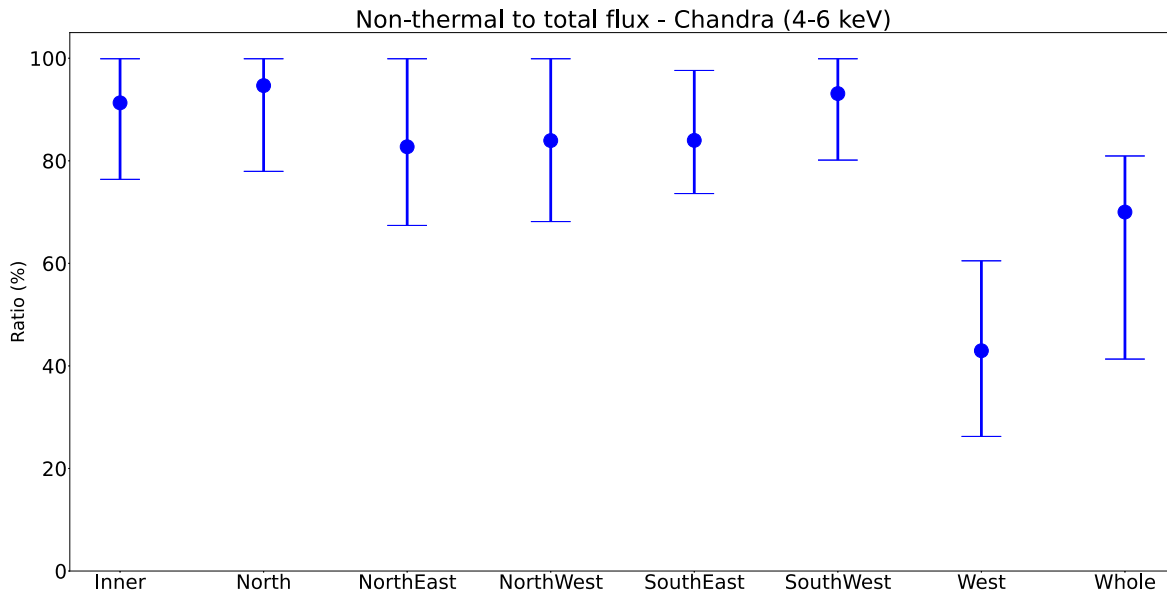
**Figure 10.** Ratios of nonthermal to total flux in the 4–6 keV band obtained from the fits in the 0.5–8 keV band as a function of the region.

up to 40 keV, we selected regions with a characteristic size at least comparable to the NuSTAR PSF (∼60″ in half power diameter). It was then natural to expect significant shocked ejecta signatures in the extracted spectra. This additional thermal contribution is added to the putative nonthermal cutoff that is therefore blurred out.

A partial solution for this issue is to measure the nonthermal and the thermal flux from Chandra/ACIS-S best-fit models performed in the 0.5–8 keV band. We modeled the Chandra/ACIS-S data with a model made of an absorbing component, `TBabs` model in XSPEC, a power law, and a number of `vnei` components, depending on the complexity of the plasma thermal emission. Given the extremely high number of counts in the spectra extracted from regions I, W, and "whole," we included systematic errors of 3%, 3%, and 5%, respectively, during the fitting procedure. We measured the total and the nonthermal-only flux through the `cflux` component available within XSPEC. Figure 10 shows the ratios of nonthermal to total flux for all of the regions considered.

All of the regions, except for the west and "whole" regions, showed a nonthermal to total flux ratio higher than 80%, and consistent with 100%. Lower values found for the west and "whole" regions were not surprising, since in these regions significant emission from shocked ejecta was revealed in previous works (e.g., Hwang & Laming 2012). These results confirmed that not including a thermal component when fitting 4–6 keV energy range had a small to nonexistent effect on the estimate of the slope of the spectra. It is worth mentioning that the values displayed in Figure 10 did not provide information on the shape of the photon spectra because of the degeneracy between emission measure and abundance (see Greco et al. 2020 for details). In fact, by repeating the analysis with pure-ejecta components, i.e., `vnei` models with abundances values fixed to $\gtrsim 10^3$, the ratio increased by reaching values of 95%, as also reported by Vink et al. (2022b).

# Appendix E
# Plots for All of the Regions

In this section we present the plots described in Figures 7–9 for all of the regions considered in this analysis (Figures 11–13, respectively).
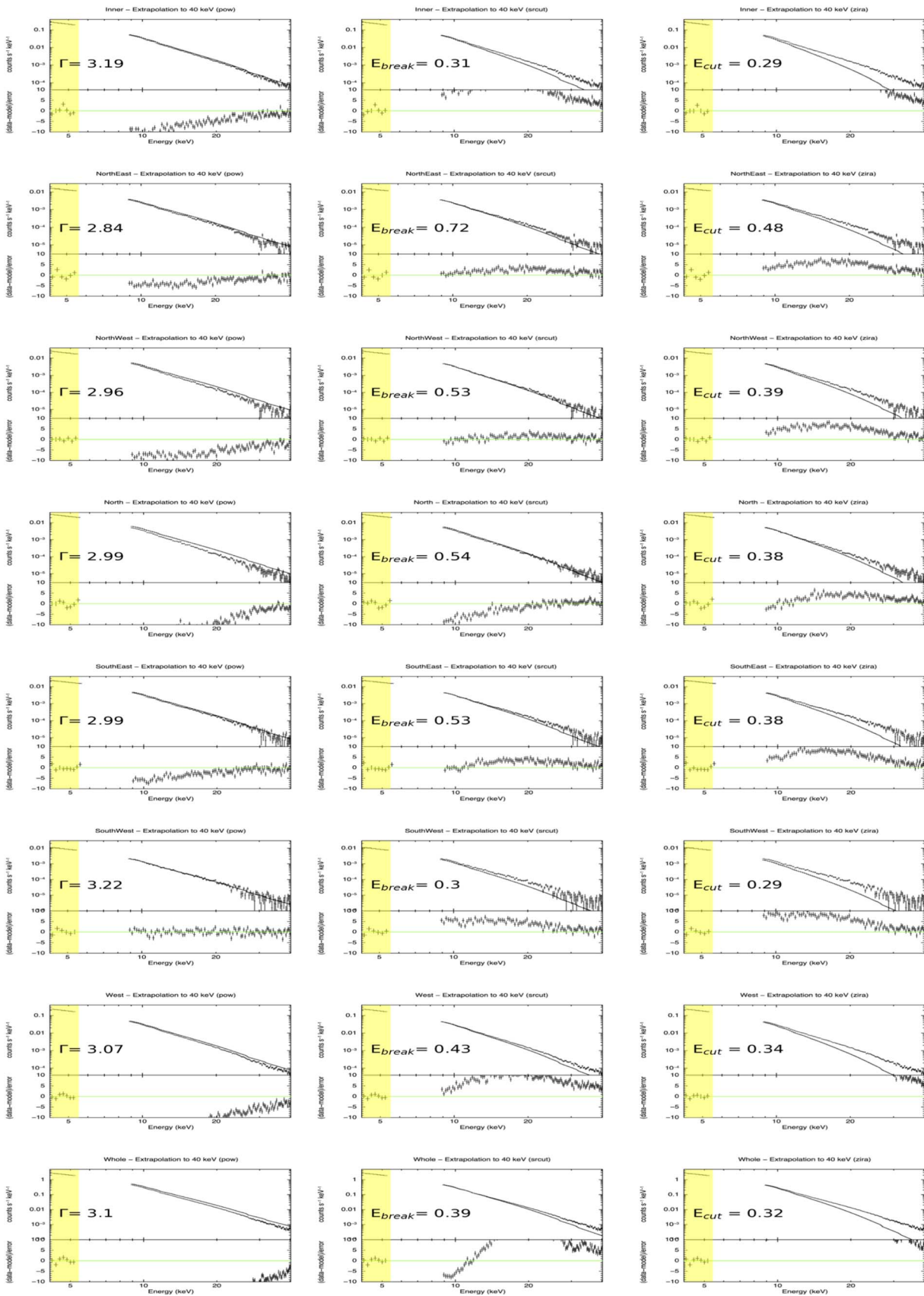
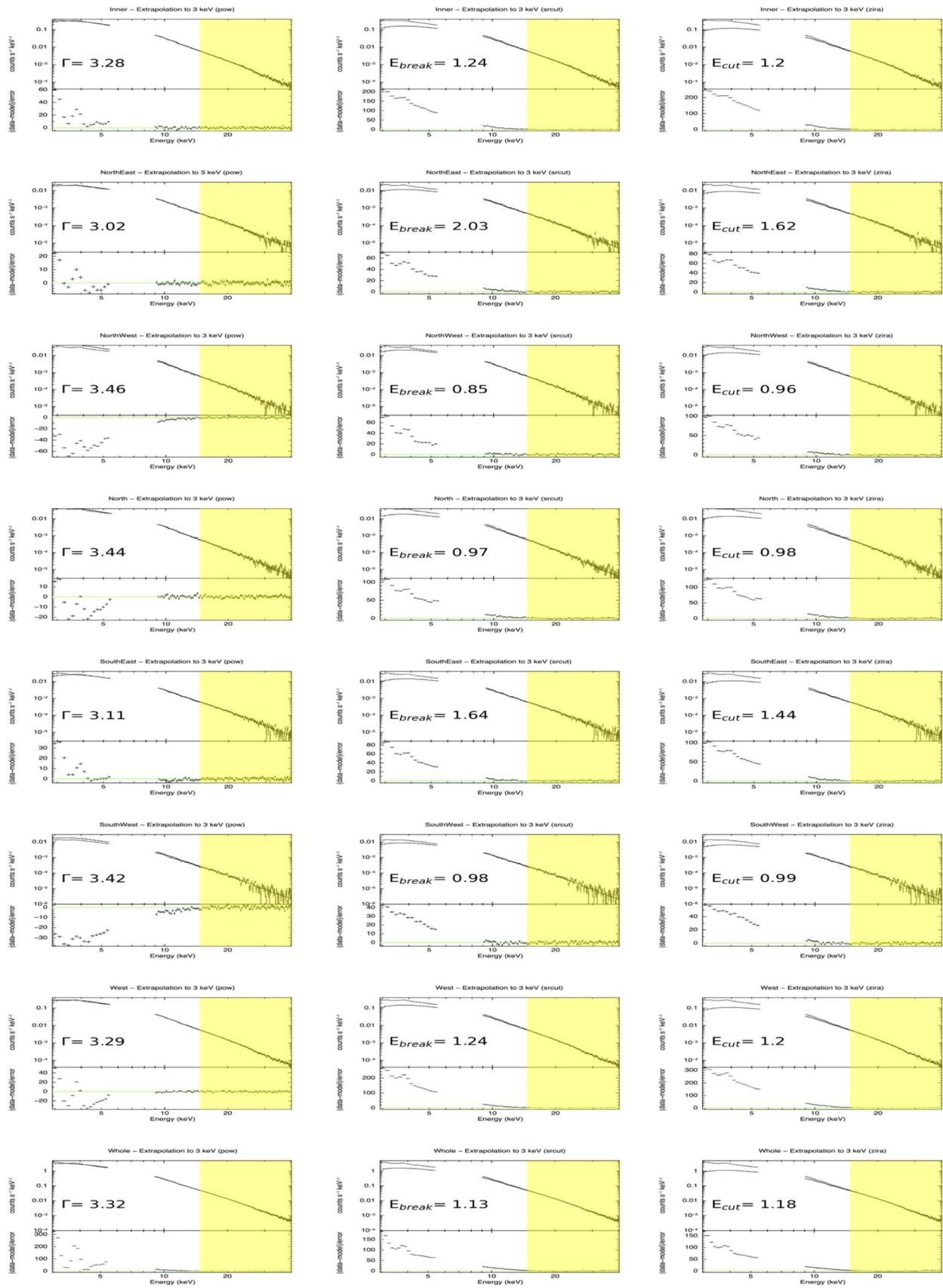**Figure 11.** Same as Figure 7 but for all of the regions considered.

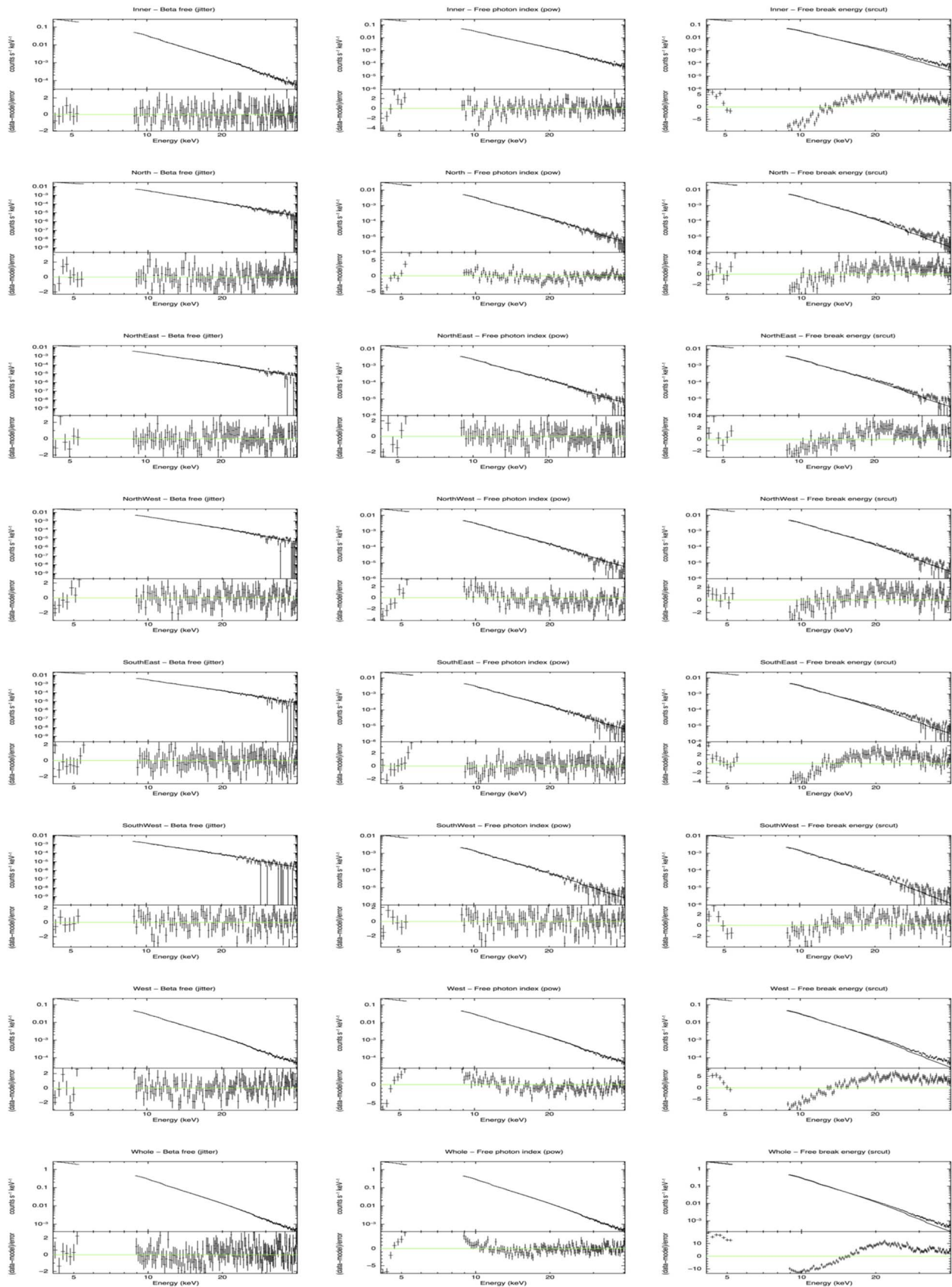**Figure 12.** Same as Figure 8 but for all of the regions.

**Figure 13.** Same as Figure 9 but for all of the regions.

## ORCID iDs

Emanuele Greco ⓘ https://orcid.org/0000-0001-5792-0690
Jacco Vink ⓘ https://orcid.org/0000-0002-4708-4219
Amael Ellien ⓘ https://orcid.org/0000-0002-1038-3370
Carlo Ferrigno ⓘ https://orcid.org/0000-0003-1429-1059

## References

Ahnen, M. L., Ansoldi, S., Antonelli, L. A., et al. 2017, MNRAS, 472, 2956
Akaike, H. 1974, ITAC, 19, 716
Allen, G. E., Keohane, J. W., Gotthelf, E. V., et al. 1997, ApJL, 487, L97
Arnaud, K. A. 1996, in ASP Conf. Ser. 101, Astronomical Data Analysis Software and Systems V (San Francisco, CA: ASP), 17
Bamba, A., Yamazaki, R., Yoshida, T., Terasawa, T., & Koyama, K. 2005, ApJ, 621, 793
Barthelmy, S. D., Barbier, L. M., Cummings, J. R., et al. 2005, SSRv, 120, 143
Bell, A. R. 1978, MNRAS, 182, 147
Berezhko, E. G., & Völk, H. J. 2004, A&A, 419, L27
Bykov, A. M., Ellison, D. C., Osipov, S. M., Pavlov, G. G., & Uvarov, Y. A. 2011, ApJL, 735, L40
Cassam-Chenaï, G., Hughes, J. P., Ballet, J., & Decourchelle, A. 2007, ApJ, 665, 315
Courvoisier, T. J. L., Walter, R., Beckmann, V., et al. 2003, A&A, 411, L53
Domček, V., Vink, J., Hernández Santisteban, J. V., DeLaney, T., & Zhou, P. 2021, MNRAS, 502, 1026
Ferrazzoli, R., Slane, P., Prokhorov, D., et al. 2023, ApJ, 945, 52
Garmire, G. P., Bautz, M. W., Ford, P. G., Nousek, J. A., & Ricker, G. R. J. 2003, Proc. SPIE, 4851, 28
Ginzburg, V. L., & Syrovatskii, S. I. 1965, ARA&A, 3, 297
Giuffrida, R., Miceli, M., Caprioli, D., et al. 2022, NatCo, 13, 5098
Greco, E., Vink, J., Miceli, M., et al. 2020, A&A, 638, A101
Green, D. A. 2019, JApA, 40, 36
Grefenstette, B. W., Fryer, C. L., Harrison, F. A., et al. 2017, ApJ, 834, 19
Grefenstette, B. W., Harrison, F. A., Boggs, S. E., et al. 2014, Natur, 506, 339
Grefenstette, B. W., Reynolds, S. P., Harrison, F. A., et al. 2015, ApJ, 802, 15
Harrison, F. A., Craig, W. W., Christensen, F. E., et al. 2013, ApJ, 770, 103
Helder, E. A., Vink, J., Bykov, A. M., et al. 2012, SSRv, 173, 369
Hwang, U., & Laming, J. M. 2012, ApJ, 746, 130
Kaastra, J. S., & Bleeker, J. A. M. 2016, A&A, 587, A151

Kelner, S. R., Aharonian, F. A., & Khangulyan, D. 2013, ApJ, 774, 61
Kolmogorov, A. 1941, DoSSR, 30, 301
Kraichnan, R. H. 1965, PhFl, 8, 1385
Lebrun, F., Leray, J. P., Lavocat, P., et al. 2003, A&A, 411, L141
Li, J.-T., Ballet, J., Miceli, M., et al. 2018, ApJ, 864, 85
Longair, M. S. 2011, High Energy Astrophysics (Cambridge: Cambridge Univ. Press)
Lucy, L. B. 1974, AJ, 79, 745
Madsen, K. K., Forster, K., Grefenstette, B., Harrison, F. A., & Miyasaka, H. 2022, JATIS, 8, 034003
Madsen, K. K., Harrison, F. A., Markwardt, C. B., et al. 2015, ApJS, 220, 8
Malkov, M. A., & O'C Drury, L. 2001, RPPh, 64, 429
Miceli, M., Bocchino, F., Decourchelle, A., et al. 2013, A&A, 556, A80
Neronov, A., Savchenko, V., Tramacere, A., et al. 2021, A&A, 651, A97
Orlando, S., Wongwathanarat, A., Janka, H. T., et al. 2022, A&A, 666, A2
Picquenot, A., Williams, B. J., Acero, F., & Guest, B. T. 2023, A&A, 672, A57
Pohl, M., Yan, H., & Lazarian, A. 2005, ApJL, 626, L101
Prosekin, A. Y., Kelner, S. R., & Aharonian, F. A. 2016, PhRvD, 94, 063010
Reed, J. E., Hester, J. J., Fabian, A. C., & Winkler, P. F. 1995, ApJ, 440, 706
Renaud, M., Vink, J., Decourchelle, A., et al. 2006, ApJL, 647, L41
Reville, B., & Kirk, J. G. 2010, ApJ, 724, 1283
Reynolds, S. P. 1996, ApJL, 459, L13
Reynolds, S. P., Borkowski, K. J., Green, D. A., et al. 2008, ApJL, 680, L41
Reynolds, S. P., & Keohane, J. W. 1999, ApJ, 525, 368
Richardson, W. H. 1972, JOSA, 62, 55
Sapienza, V., Miceli, M., Bamba, A., et al. 2022, ApJ, 935, 152
Schwarz, G. 1978, AnSta, 6, 461
Takabe, H. 2023, PhPl, 30, 030901
The, L. S., Leising, M. D., Kurfess, J. D., et al. 1996, A&AS, 120, 357
Toptygin, I. N., & Fleishman, G. D. 1987, Ap&SS, 132, 213
Tsuji, N., Uchiyama, Y., Khangulyan, D., & Aharonian, F. 2021, ApJ, 907, 117
Vink, J. 2020, Physics and Evolution of Supernova Remnants (Berlin: Springer)
Vink, J., & Laming, J. M. 2003, ApJ, 584, 758
Vink, J., Patnaude, D. J., & Castro, D. 2022a, ApJ, 929, 57
Vink, J., Prokhorov, D., Ferrazzoli, R., et al. 2022b, ApJ, 938, 40
Wang, W., & Li, Z. 2016, ApJ, 825, 102
Weisskopf, M. C., Soffitta, P., Baldini, L., et al. 2022, JATIS, 8, 026002
Zirakashvili, V. N., & Aharonian, F. 2007, A&A, 465, 695